Electronic quality factor control for piezoelectric transducer arrays

T. F. Wemelsfelder

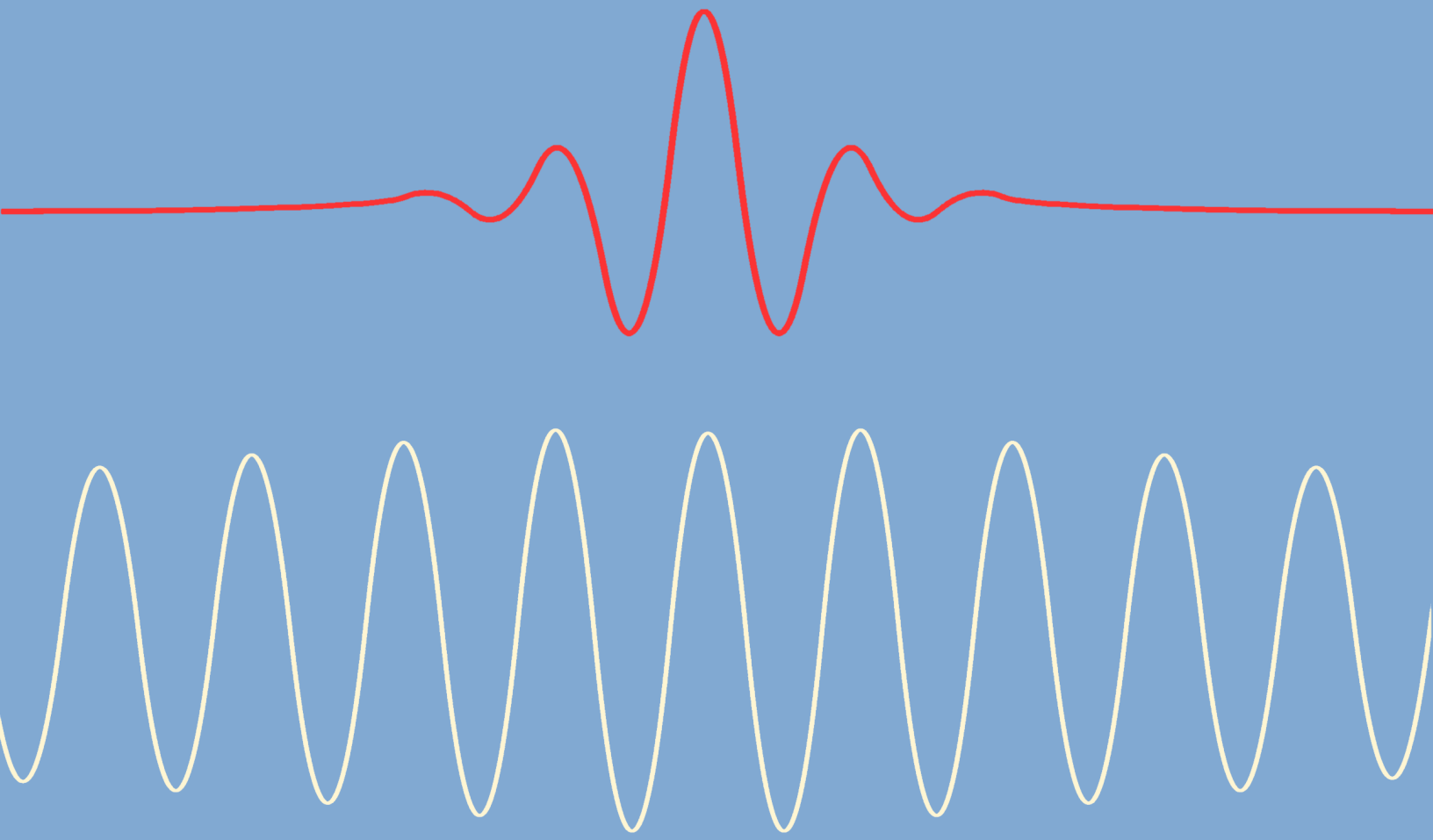

TU Delft

Electronic quality factor control for piezoelectric transducer arrays

by

T.F. Wemelsfelder

to obtain the degree of Master of Science in Biomedical Engineering
at the Delft University of Technology,
to be defended publicly on Friday February 23, 2024 at 13:00.

Student number: 4492226
Project duration: Dec 2022 - Feb 2024

Thesis supervisor:	Dr. T. Costa	
Thesis commitee:	Dr. T. Costa	Chair
	Dr. T. Manzaneque	

TU Delft

Abstract

In recent years, many therapeutic applications for medical ultrasound have arisen, such as ablation of tumors, breaking up kidney stones, and neuromodulation. To localize the target area, often ultrasound imaging methods are used. Conventionally, a different transducer array is used for imaging and therapeutic applications because of their conflicting requirements of transducer damping. If this damping would be done electronically, it can be switched on or off on demand, allowing a single transducer array to be used for both therapeutic and imaging ultrasound. This would allow medical ultrasound devices to be smaller and therapeutic treatments to have reduced overall system complexity. This thesis develops a PCB to compare a combination of existing and novel methods of electronic damping on a single transducer, also called electronic Q-factor control. A maximum damping of 23% is achieved relative to the undamped transducer mounted on the PCB. This is achieved by a novel method based on a feedback loop around a second 'dummy' transducer. Methods of electronic Q-factor control should eventually be extended to be applied in an Integrated Circuit for damping of entire ultrasound transducer arrays.

Contents

1 Introduction **2**

2 Background **4**
2.1 Medical Ultrasound . . . 4
2.1.1 Ultrasound imaging . . . 5
2.1.2 Therapeutic ultrasound . . . 7
2.2 Ultrasound transducers . . . 7
2.3 Equivalent electrical model . . . 9
2.3.1 Summary . . . 13
2.4 Damping techniques . . . 13
2.4.1 Shunt damping . . . 13
2.4.2 Damping by modified driving waveform . . . 14
2.4.3 Feedback . . . 14
2.5 Summary . . . 15

3 Damping method design **16**
3.1 Equivalent model parametrization . . . 16
3.1.1 Method . . . 16
3.1.2 Measurement setup and preparation . . . 18
3.1.3 Results . . . 18
3.2 Damping optimization . . . 20
3.2.1 Counterpulse system . . . 20
3.2.2 Shunt damping . . . 21
3.2.3 Proposed feedback Q-control method . . . 25
3.3 Summary . . . 27

4 System development **28**
4.1 System design . . . 28
4.2 System implementation . . . 30
4.2.1 Circuit implementation . . . 30
4.2.2 Transducer mounting (D, G) . . . 32
4.2.3 Watertight coating (G) . . . 32
4.2.4 Water tank (G) . . . 33
4.2.5 FPGA programming (A) . . . 34

5 Results **37**
5.1 Test setup . . . 37
5.2 Test results . . . 37
5.3 Discussion . . . 42

6 Conclusion **43**

A Altium circuit designs **44**

Chapter 1

Introduction

Ultrasound is a form of sound wave that exists beyond the range of human hearing, typically above 20,000 Hz. Interestingly, many animals, like dogs, cats, dolphins and bats, possess the ability to hear outside of this range. The latter two are known to utilize this capacity for echolocation to gather information about their surroundings. They produce short ultrasound clicks and listen to the reflections caused by their environment. Based on this information they can reconstruct a mental 3D image map of their surroundings. This is the natural occurrence of a process called ultrasound imaging.
Ultrasound imaging is used by humans mostly in the medical field; Most famously for getting an ultrasound scan during pregnancy [1], but also to assess heart function, localize internal injuries, or to guide as a visual aid during surgery.
Besides imaging, ultrasound knows another application called therapeutic focused ultrasound (FUS). This technique uses a multitude of ultrasound transducers to send long high intensity waves to focus their combined energy into a single point. FUS is used in varying applications, such as ablation of tumors, breaking up kidney stones, and modulation of neural activity [2, 3]. Therapeutic ultrasound can be combined with ultrasound imaging to determine the desired focal spot. Current conventional methods use a different device for imaging and therapeutic applications [4], or use an imaging array for both, resulting in very inefficient performance during therapeutic use [5]. Especially for wearable neuromodulation applications and research it is desirable to have a single device capable of delivering optimal performance in both cases. Firstly, using the same ultrasound array for both imaging and modulation would greatly help reduce the total product size, making it less cumbersome and much easier to mount on any test subject. Furthermore having a single device would allow stimulating and imaging from the exact same location, reducing complexity and inaccuracy as compared to separated devices. Currently, imaging and therapeutic modes are not interchangeable because of their fundamentally different properties: In order to achieve very short ultrasound pulses, ultrasound imaging arrays use mechanical damping layers situated directly behind the transducer, while therapeutic arrays use air-backing for minimal damping and minimal energy loss. For this reason it is desirable to design an electronic damping circuit towards achieving control of the quality factor (Q-factor): For a device capable of both imaging and therapeutic ultrasound, the air-backed transmitter transducers (TX) will be connected to an electronic Q-factor control circuit allowing switching between high Q-factor (therapeutic, low damping) and low Q-factor (imaging, high damping). The receive transducers (RX), only required for imaging mode, will sparsely populate the transducer array, and can be damped with conventional mechanical layers. With these features, the electronic damping can be switched on or off on demand, and thus allow for the fast switching between imaging and therapeutic operation using just a single transducer array. This thesis will answer the question whether it is feasible to apply electronic Q-factor control circuits to air-backed transmitters in an ultrasound transducer array, as to allow for both imaging and therapeutic applications in a single device. To answer this question, this this work analyzed several different Q-factor control circuits proposed in prior work, and proposed a novel technique that might enable its use, for the first time, in high-density 2D arrays of ultrasound

transducers.
This thesis is organized as follows. In chapter 2 a literature review is given for the fields of ultrasound applications and piezoelectric transducers. Chapter 3 optimizes and extends existing methods for Q-factor control to allow for implementation in ultrasound transducer arrays based on an equivalent electrical transducer model. Q-factor control systems are simulated in Matlab and LTSpice. In chapter 4 a full PCB system is developed which is able to apply several damping techniques on a real transducer placed in a small water tank. Chapter 5 presents hydrophone measurements of the PCB and discusses the results. Chapter 6 will provide the final conclusion for this thesis and provide recommendations for future work.

Chapter 2

Background

2.1 Medical Ultrasound

Ultrasound transducers allow for the conversion of electrical energy to acoustical ultrasound vibrations. Upon actuation a sound wave will travel in all directions from the transducer, however typical medical ultrasound applications require the ability to precisely focus the acoustic energy in a single point. The focusing of ultrasound is done using arrays of multiple transducers. By actuating each transducer element at a slight offset in time, a phase delay, their acoustical waves can be made to arrive at a single point simultaneously, the focal point. This is called constructive interference, shown in figure 2.1. Using different phase delays, the location of the focal spot can be changed.

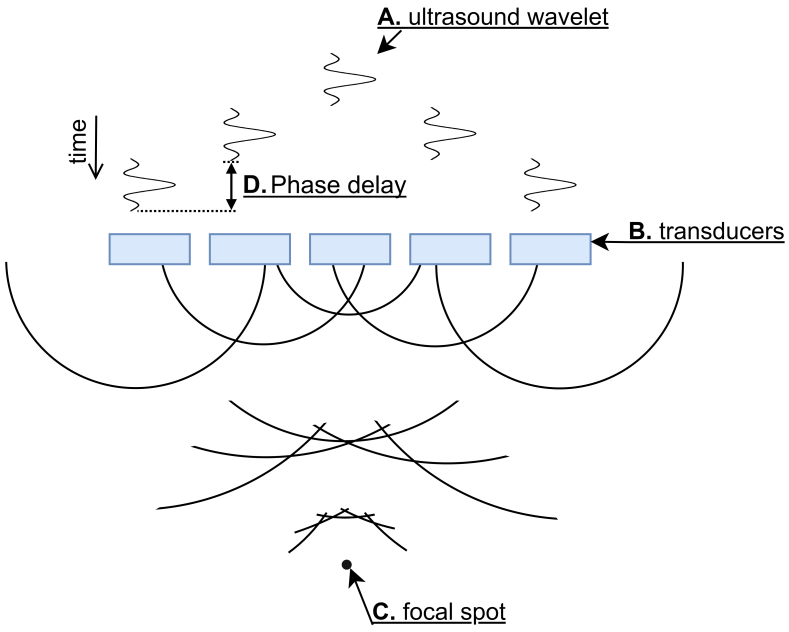

Figure 2.1: Visualization of a linear phased array. The same shape ultrasound wavelet (**A.**) is emitted by the transducers (**B.**) at different times, which is called a phase delay (**D.**). Based on the phase delay, the acoustic energy is focused on a single spot, called the focal spot (**C.**).

Focused ultrasound (FUS) is used both for imaging and stimulation purposes. Where imaging methods require very short acoustic waves to maximize axial resolution, stimulation purposes need

minimally damped, long duration waves to maximize energy delivery. This can also be referred to by means of the quality factor, or Q-factor. In ultrasound applications, it is mathematically defined as the ratio of the center frequency to the signal bandwidth:

$$Q = \frac{f_c}{B} \tag{2.1}$$

The Q-factor is a measure of the level of damping of an ultrasound transducer, and it corresponds approximately to the amount of oscillations in a vibration before it dies out. For an input step voltage, a high-factor transducer will resonate for a longer time, while a low Q-factor transducer will resonate for a shorter time. A stimulation array requires high Q-factor transducers, while an imaging array needs a low Q-factor. Both are visualised in figure 2.2. It can be seen that lower damping results in a narrower peak in the frequency domain, while a shorter wave gives a wide frequency band. In this discrepancy between imaging and stimulation mode lies the challenge of this thesis, where the goal is to design, build and verify electronic methods to allow ultrasound transducers to switch between both operating modes.

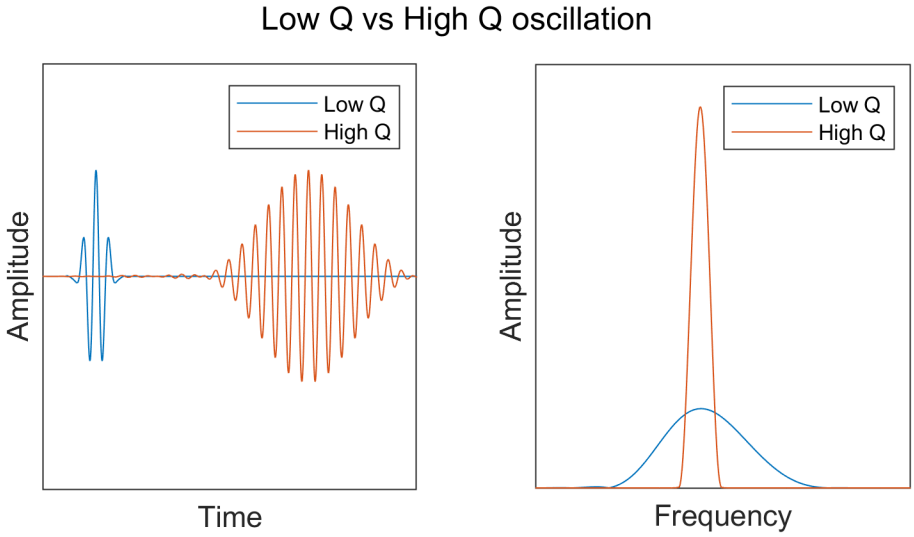

Figure 2.2: Highly damped signal (low Q, blue) and less damped signal (high Q, red) in the time domain (*left*) and frequency domain (*right*).

2.1.1 Ultrasound imaging

Ultrasound imaging is commonly used for recording 3D images of biological tissue. A multitude of methods exist to reconstruct images and gather data from ultrasonic reflections. Common modes are B-mode (Brightness mode) for black and white 2-D and 3-D images, CEUS (contrast enhanced ultrasound) for visualizing blood flow and lesions with the aid of a contrast enhancing agent injected into the bloodstream, and Doppler mode for measuring blood flow velocity. All modes can be executed using the same type of transducer array shown in figure 2.3, but the type of wave transmitted may vary. To produce high resolution static or low framerate images, a focused beam is transmitted by the transducer array to produce an image line-by-line as shown in figure 2.4. In contrast to focused imaging, for applications such as CEUS or Doppler mode very high framerates can be achieved with the use of plane wave imaging. Instead of creating a focal spot by means of phase delay as shown in figure 2.1, the transmitted wave will be unfocused, for example by setting all phase delays to zero. Focusing is then done in the signal processing stage, after reception of the reflected waves. The resolution in

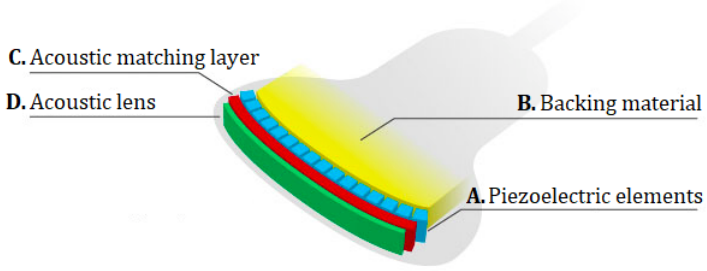

Figure 2.3: Basic elements of a conventional ultrasound imaging array. The piezoelectric elements (**A.**) will be driven by an electrical circuit to start oscillating. This vibration is damped by the backing material (**B.**). The acoustic matching layer (**C.**) facilitates maximal power transfer from the piezoelectric elements into the tissue to be imaged. The acoustic lens (**D.**) helps with focusing the ultrasound pulses of the individual transducer elements. *Image adapted from [6]*

each point of the image is based on different parameters. The lateral resolution is determined by focal distance F, aperture size D and the wavelength λ in the medium.

$$R_{lateral} = \lambda \frac{F}{D} \tag{2.2}$$

Where the aperture size is the length of the transducer array used for either transmission in focused ultrasound or reception in unfocused ultrasound. The transducer elements will have a natural focal spot in the elevational plane determined by their width $h_{element}$:

$$F \approx \frac{0.34 h_{element}^2}{\lambda} \tag{2.3}$$

At this distance, the slice thickness is equal to

$$R_{elevational} \approx 0.6 h_{element} \tag{2.4}$$

The axial resolution follows from the properties of the transmitted wave as

$$R_{axial} = \frac{w}{2} = \frac{c\tau}{2} \tag{2.5}$$

where w is the physical width of the ultrasound wave, c is the speed of sound through the medium and τ is the duration of the wavelet. In the axial plane, two points can be identified as separate objects when their reflected waves do not overlap at the moment of reception, as shown in figure 2.5. Because the wave must travel to the point and back again, the time delay between the reception of a reflection of two points separated by distance Δz is twice this distance divided by the sound velocity. The points can only be distinguished when this time delay is greater than the temporal length of the reflected wave in the medium. This is mathematically expressed as

$$\Delta t = 2\Delta z / c > \tau \tag{2.6}$$

The axial resolution is then the lowest acceptable Δz, which leads to equation 2.5. It is clear that the shorter the wave, the higher the axial resolution. This is why it is important to achieve high damping for ultrasound imaging applications. A trade-off is however that for a shorter wave duration, the wave will contain less energy. In imaging this means the reflections will be of lower energy as well and thus the signal to noise ratio (SNR) is reduced.

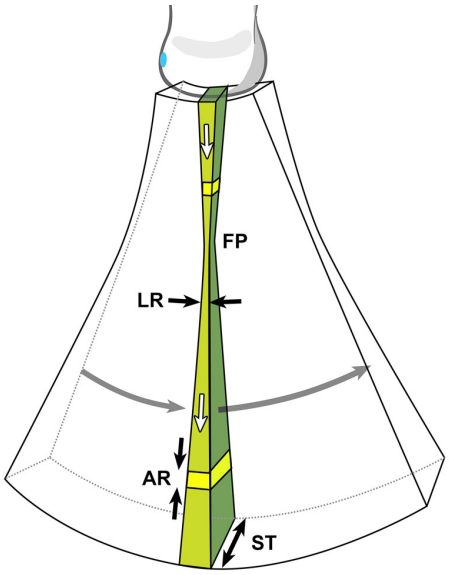

Figure 2.4: A linear transducer array is able to sweep over an arc to sample three dimensional voxels. The voxel size is determined by the lateral resolution (**LR**), elevational resolution i.e. slice thickness (**ST**) and axial resolution (**AR**). Resolution is highest at the focal point (**FP**). *Image taken from [7]*

2.1.2 Therapeutic ultrasound

Where ultrasound imaging is an observation method, therapeutic ultrasound is used in the medical field to actively provide treatment to patients in many different ways. The fundamental principle of energy focusing is the same as shown in figure 2.1, however in therapeutic applications it is generally not desirable to produce very short duration pulses. Waves for therapeutic ultrasound are much longer and of higher intensity in comparison, with the purpose of delivering as much energy as possible to the focal point with minimum losses. Herein also lies a fundamental difference with imaging modes: Whereas imaging arrays make use of the mechanical backing layer as shown in figure 2.3, transducers used for stimulation often make use of air-backing in order to minimize damping and maximize reflection [9]. Focused ultrasound encompasses two main subgroups: High Intensity Focused Ultrasound (HIFU) and Low Intensity Focused Ultrasound (LIFU). HIFU is specifically meant to damage or destroy biological tissue with intensities ranging from 100 to 10,000W/cm^2 [2]. It is used among others for the ablation of tumors and breaking up kidney stones[2][10]. LIFU, on the contrary, uses intensities from 100W/cm^2 down to the mW/cm^2 range to stimulate tissue repair [11] or to elicit neurological activity [12]. To determine the desired focal spot, ultrasound imaging methods can be used. Current methods either use two separate arrays optimized for either stimulation or imaging mode [4], or use a single imaging array to do both, resulting in very inefficient performance during stimulation [5]. To solve this issue it is desirable to be able to use a single array which can switch between one mode optimized for imaging, and one mode optimized for stimulation.

2.2 Ultrasound transducers

Ultrasound transducers are the elements used to generate ultrasound. They can convert electrical energy to mechanical ultrasonic vibrations, or vice-versa. As such they are both used as sensors as well as actuators. A multitude of materials can be used to generate ultrasound, such as capacitive and piezoelectric micromachined ultrasound transducers (CMUT and PMUT), and piezo-electric ceramic. A common material used for ultrasound transduction in medical devices is lead zirconate titanate, also

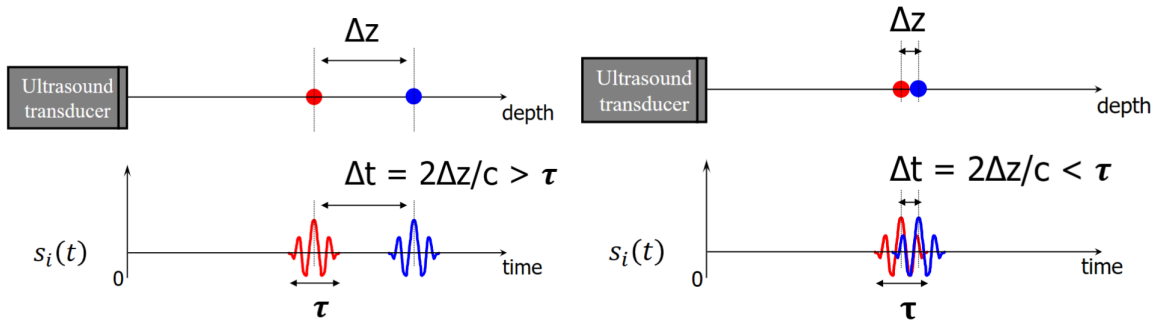

Figure 2.5: *left* Two points are identifiable as different objects because their reflected waves do not overlap. *right* The two points are closer together than half the wavelet width ($\Delta z < c\tau/2$) and therefore they cannot be distinguished from each other. *Images from [8]*

called PZT [13], a piezo-electric ceramic with a crystalline structure. Piezo-electric crystals owe their piezo-electric effect to their repeating structures containing positively and negatively charged atoms. When the material is under no stress, the charge distribution of the individual atoms is balanced, and no voltage can be measured over the crystal as a whole. However when the crystal is stretched or compressed, the charge distribution changes resulting in a net voltage over the crystal faces. The reverse relationship also applies: by applying a voltage over its faces, the shape of a piezo-electric crystal can be deformed. The piezo-electric effect is demonstrated in figure 2.6 for a simple crystalline structure. A real crystal will be comprised of a lattice of many repetitions of this structure in 3D space. The deformation of such crystals used for ultrasound transduction is underdamped, i.e. when applying

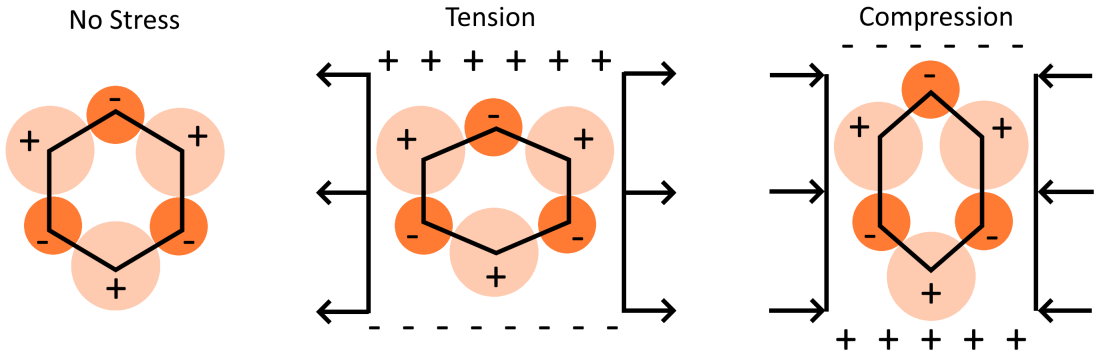

Figure 2.6: A visualization of the piezo-electric effect. The images show a crystal comprised of positively and negatively charged atoms. With no applied forces, the charge distribution is exactly balanced and there is no net voltage over the crystal. However when the crystal is deformed by tension or compression, indicated by the arrows, this causes the displacement of atoms in the crystal, and a net voltage will arise over the crystal faces. *Image adapted from [14]*

a step voltage they will vibrate at a natural frequency before settling. This is exactly the vibration that is exploited for creating ultrasound waves: the deformation of the crystal causes pressure waves in its contact medium and sound is created. The natural frequency -also called resonant frequency- depends on the material used, but also on its shape and the direction in which the voltage is applied. We can refer to the combination of the latter two as the vibrational mode. A piezo-electric material can expand and compress in many directions, however for ultrasound transducers mainly two modes

are of interest: thickness mode and longitudal mode, as visualized in figure 2.7. In longitudal mode, the resonant frequency decreases with increasing transducer length [15], while in thickness mode the resonant frequency decreases with increasing surface area [16]. It is clear that the behaviour of a

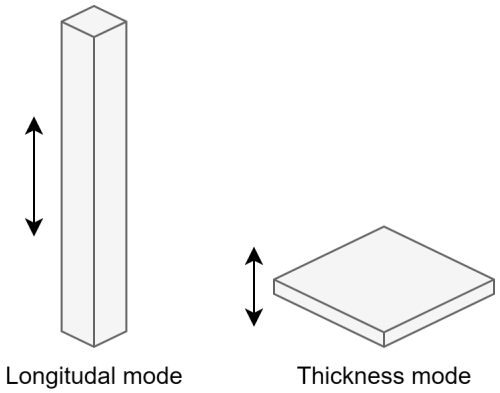

Figure 2.7: Illustration of the two main vibrational modes for ultrasound piezo-electric transducers. In longitudal mode the transducer deforms along its length, while in thickness mode it deforms along its shortest dimension.

piezo-electric crystal depends on many factors. To simplify the analysis of these transducers, the next section will cover how to encompass their behaviour in an equivalent electrical model.

2.3 Equivalent electrical model

To design a good system it is necessary to have accurate simulations. Models are used to simulate these systems before they are built, however, models will never be able to perfectly represent the reality. Depending on the application, a model may require increased precision, or take into account different parameters. For piezo-electric transducers it is just the same. In order to design an electrical damping method for piezo-electric transducers, it is essential to firstly have a way to model the transducer in the electrical domain. This section will evaluate several models from simple to complex, each with their advantages and disadvantages.

The piezo-electric transducer is most simply modeled as a single capacitor C_0, the physical capacitance of the piezo-electric material. The value of C_0 can be derived from the material properties according to

$$C_0 = \epsilon_0 \epsilon_r \frac{A}{d} \tag{2.7}$$

Where ϵ_0 is the electric constant, ϵ_r the dielectric constant, A is the surface area of the transducer top/bottom face and d is traditionally the distance between the capacitor plates, or in this case the thickness of the transducer. A single capacitor however is not a sufficient model to represent a transducer's natural resonant behaviour.
Exact electrically equivalent circuits for piezo-electric transducers were published by Mason et al. in 1948 [15]. From the mechanical properties of piezo-electric materials, a set of equations is derived which can be represented in a non-linear electrical model shown in figure 2.8. In this model, the resonant behaviour of a transducer is represented by the non-linear impedances over the entire frequency range, showing that resonant peaks occur at all uneven harmonics of the primary resonant frequency ω_0.

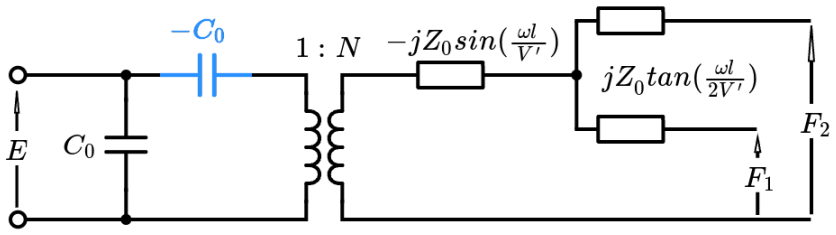

Figure 2.8: Mason's equivalent model displays that the transducer can exert force both at its front and at its back side, represented by F_1 and F_2. Non-linear impedances are dependant on the frequency ω, as well as the mechanical constants Z_0, l, and V'. l being the crystal longitudal dimension, Z_0 the mechanical impedance and V' the wave velocity through the crystal. The transformer is an ideal transformer with ratio 1 to N defining the force to voltage ratio. C_0 is the physical capacitance of the transducer material. For thickness mode vibration the negative capacitance (in light blue) is added to model a change in resonant frequency with respect to longitudal mode, for transverse longitudal vibration it is a short circuit [17]. The input voltage is represented by E.

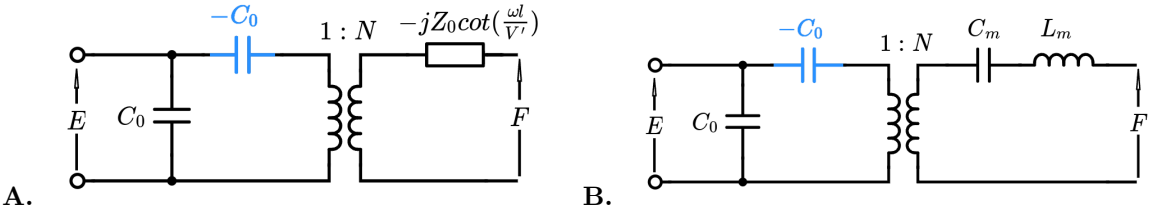

Figure 2.9: **A.** Equivalent circuit for a transducer clamped on one side. **B.** Approximation in the vicinity of the primary resonance frequency.

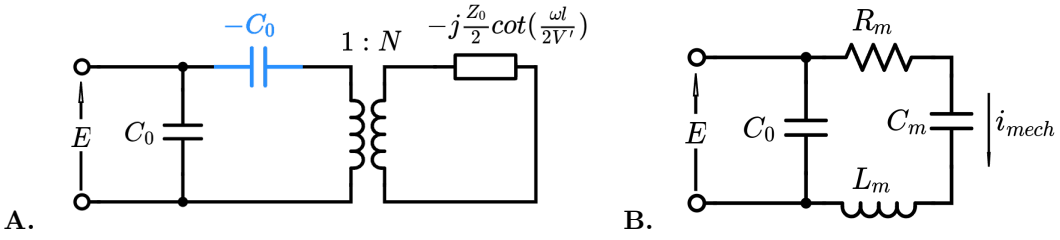

Figure 2.10: **A.** Equivalent circuit for a transducer resonating in free space. **B.** Approximation in vicinity of the primary resonant frequency. Resistor R_m is added to represent internal mechanical losses. i_{mech} is the current through the RLC branch, proportional to the transducer velocity. The resonant frequency will be differ between transverse longitudal and thickness vibration mode.

One problem with this representation is that non-linear behaviour can be difficult to simulate. The model can be simplified for cases where one side is clamped (no vibration possible), or one or both sides are unloaded (no force transfer). For the first case, the clamped side force can be set to infinity, i.e. an open circuit, resulting in figure 2.9A. The result can be approximated in a linear representation with only one resonant frequency, see figure 2.9B. In the case where both sides of the transducer are moving in free space, this means both F_1 and F_2 of figure 2.8 should be set to zero, as there is no force transfer possible. This equals to short-circuiting both force ports resulting in circuit A of figure

2.10. Note that the resonant frequency is twice as high with respect to the clamped representation in figure 2.9. The non-linear impedance can be approximated around the primary resonant frequency by a lumped element model seen in figure 2.10B. This one-port representation is also known as the Butterworth-van Dyke model, or BVD model. When the transducer is excited by a voltage, it expands and contracts. This means the free (unclamped) end of the transducer will start to experience an oscillating displacement in space, causing a pressure difference in the surrounding medium. In the BVD model, the velocity of this free end's movement is proportional to the current i_{mech} running through the RLC branch [18]. The transducer impedance is equal to

$$Z_{eq} = \frac{s^2 C_m L_m + s C_m R_m + 1}{s^3 C_o C_m L_m + s^2 C_o C_m R_m + s(C_o + C_m)} [\Omega] \tag{2.8}$$

and the current through the RLC branch follows the equation

$$i_{mech} = E \frac{s C_m}{s^2 L_m C_m + s C_m R_m + 1} [A] \tag{2.9}$$

where E is the voltage over the transducer. From the circuit it follows that there is minimum impedance where $Z_{L_m} + Z_{C_m} = 0$. So $j\omega_0 L_m + \frac{1}{j\omega_0 C_m} = 0$ and thus

$$\omega_0 = \frac{1}{\sqrt{L_m C_m}} \tag{2.10}$$

Note that equation 2.9 resembles the form of a second order band-pass filter:

$$H(s) = \frac{s\omega_0/Q}{s^2 + s\omega_0/Q + \omega_0^2} \tag{2.11}$$

where Q is the quality factor. i_{mech} can now be written as

$$i_{mech} = \frac{E}{R_m} \frac{s\omega_0/Q}{s^2 + s\omega_0/Q + \omega_0^2} = \frac{E}{R_m} \frac{s\frac{R_m}{L_m}}{s^2 + s\frac{R_m}{L_m} + \frac{1}{L_m C_m}} [A] \tag{2.12}$$

From which it follows that

$$Q = \omega_0 \frac{L_m}{R_m} = \frac{1}{R_m} \sqrt{\frac{L_m}{C_m}} \tag{2.13}$$

The BVD model shows that the resonant behaviour of a piezo-electric transducer can be analyzed using a set of simple equations, however under the assumption that the transducer is unloaded. Furthermore it does not model higher harmonic frequencies.

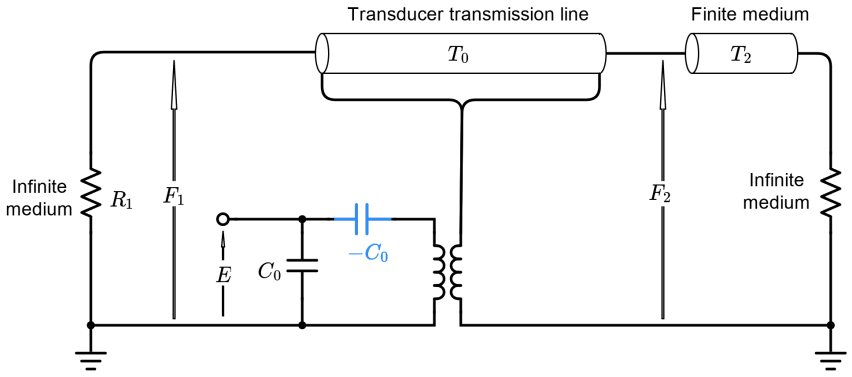

Figure 2.11: Redwood's transmission line model for a piezo-electric transducer with added mechanical coupling. The transducer's resonant behaviour is modelled by transmission line T_0. Mechanical layers and transmission media are modelled by a transmission line for finite media (T_2) or a resistor for infinite media (R_1 and R_2).

As an alternative, the Mason model was adapted by Redwood et al. by modelling the resonant part of the circuit as a transmission line [19], as shown in figure 2.11. This modification facilitates the addition of external mechanical loads (transmission media), and is able to encapsulate the transducer behaviour over a wide frequency range in a linear model. A finite transmission medium, such as a matching layer, is modelled as a lossy transmission line, while a virtually infinite medium can be modelled by a single resistor [20]. To model the acoustic impedance of a medium as electrical components, the same conversion system is used as used by Mason: Force is represented by voltage and velocity is represented by current. This gives the following convergence from acoustic impedance Z_a to electric impedance Z_{el} [20]:

$$Z_{el} \equiv Z_a A \tag{2.14}$$

Where A is the cross-sectional area of the sound wave. Following the same system, the lossy transmission line model for a finite medium consists of the following values for R, L and C per unit length [20]:

$$L \equiv \rho A \quad [H/m] \tag{2.15}$$

$$C \equiv \frac{1}{c^2 \rho A} \quad [F/m] \tag{2.16}$$

$$R \equiv 2c\rho A\alpha \quad [\Omega/m] \tag{2.17}$$

with A the contact area with the medium, ρ the medium density, c the velocity of sound through the medium and α the attenuation coefficient of the medium. For an infinite medium, the equivalent electrical resistance can be modelled by the characteristic impedance of an infinite transmission line $Z_0 = \sqrt{L/C}$ [21]. Filling in the equations for L 2.15 and C 2.16 of the lossy transmission line this results in the resistance for an infinite medium of:

$$R \equiv c\rho A \quad [\Omega] \tag{2.18}$$

In order to apply the redwood model in circuit simulators such as LTSpice, the negative capacitance and ideal transformer can be emulated by means of controlled voltage and current sources [22, 23, 20, 24]. Using the nominal T model of a transmission line [25, 26], the mechanical interface can be applied to the BVD model the same way as for the Redwood transmission line model. This results in the circuit of figure 2.12. This is the simplest transducer model that is able to simulate the resonant response of a transducer while taking into account the mechanical influence of surrounding media.

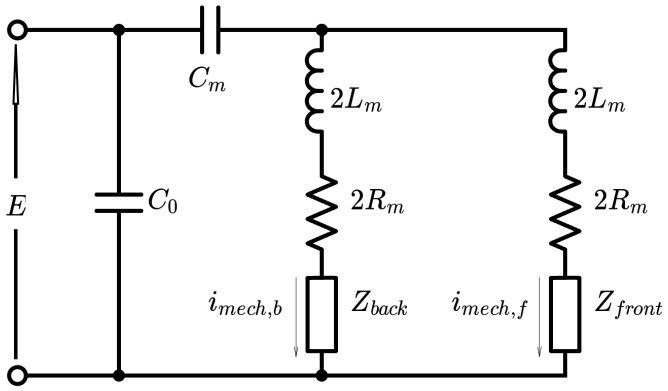

Figure 2.12: Expanded BVD-model to include front and back mechanical interface represented by Z_{front} and Z_{back}. The transducer velocities at both ends are represented by currents $i_{mech,b}$ and $i_{mech,f}$. L_m and R_m of the classical BVD-model are split between the two branches, following the nominal T model of a transmission line.

2.3.1 Summary

The Mason equivalent model is a complete model describing the relationship between the electrical and mechanical behaviour of ultrasound transducers, but its non-linear impedances make it difficult to simulate. The Redwood model is a linear derivation which is more easily applicable to simulation softwares. For analysis around the primary resonant frequency only, the BVD model, which follows from the Mason model under the assumption the transducer is in free space, is sufficient. The BVD and Redwood models can furthermore be expanded to include the mechanical influence of surrounding transmission media. The expanded BVD model can be used if mainly the primary resonant frequency is of importance, otherwise the Redwood model is more complete as it able to include all other resonant frequencies of the crystal.

.

2.4 Damping techniques

The conventional way of generating short acoustic pulses with an ultrasound imaging array is by using mechanical backing layers [27, 28]. A backing layer is placed behind the piezoelectric transducers to absorb their vibrational energy, see figure 2.3. An ultrasound array for therapeutic purposes does not need such a backing layer, as it needs to transfer as much energy as possible. If one wants to use the same transducer array for both purposes it is therefore necessary to have a damping method that can be switched on or off, which is why an *electrical* damping method will be more practical than conventional *mechanical* damping. This section will discuss already existing damping techniques in the electrical domain for ultrasound transducers.

2.4.1 Shunt damping

Shunt damping is a method commonly used in structural vibration damping to dissipate energy at selected frequencies [29, 30, 31, 32]. Shunt damping uses an impedance (shunt) connected to the piezoelectric transducer in order to absorb its energy. When the transducer starts vibrating because of electrical or mechanical excitation, the shunt will electronically dissipate the vibrational energy and thereby dampen the mechanical oscillation. For one transducer, an optimum value for the shunt exists

where it produces maximal damping at the transducer resonant frequency [18]. figure 2.13 shows a simple implementation of a transducer connected to a passive shunt.

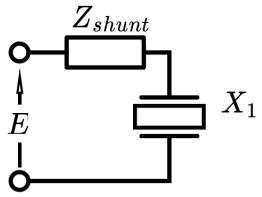

Figure 2.13: Simple implementation of a shunt damping circuit. The shunt impedance Z_{shunt} can be tuned in such a way that it maximally reduces the Q-factor of the transducer X_1.

2.4.2 Damping by modified driving waveform

The transducer vibration can be countered as well by applying a driving voltage with a specific shape. Because it is known the transducer will respond a certain way, a signal is applied that will immediately counter its movement after excitation. Previous studies have shown modified waveforms can indeed significantly increase vibrational damping [33, 34, 35]. A complex driving signal such as in [33], produced by an external signal generator, may be difficult to imitate in a real circuit implementation. The simplest driving waveform which can produce a damped response is a square pulse with a duration equal to exactly one period of the resonant frequency of the transducer [35]. A strong point of this method is that peak signal amplitude can be maintained whereas a shunt would reduce this.

2.4.3 Feedback

Studies have shown it is possible to use a piezo-electric transducer in a negative feedback loop to quickly dampen its vibration [36, 37]. A simple feedback circuit could look like figure 2.14, where a voltage proportional to the transducer movement is subtracted from the input voltage. The first step here is to

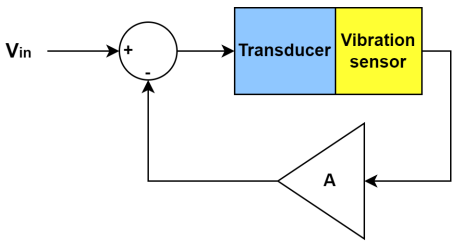

Figure 2.14: Example of a transducer in a simple feedback circuit. The transducer is set in motion by an input signal V_{in}. The vibration is sensed by the vibration sensor, which is then amplified by a factor A and subsequently subtracted from the voltage over the transducer.

acquire the vibration sensor. In [36], an off-the-shelf displacement sensor is placed on the transducer to measure its vibration. Relative to typical medical ultrasound transducers, with dimensions in the order of centimeters the displacement sensor is very large [38] and would not be feasible to implement in a medical ultrasound transducer array. Wu et al. on the other hand use an electronic sensing circuit to get a voltage proportional to the transducer velocity [37]. Such a sensor, shown in figure 2.15, has the potential to be implemented in an IC in future devices. Furthermore not only the primary resonant frequency, but also higher resonant frequencies will be represented in the sensor voltage, providing

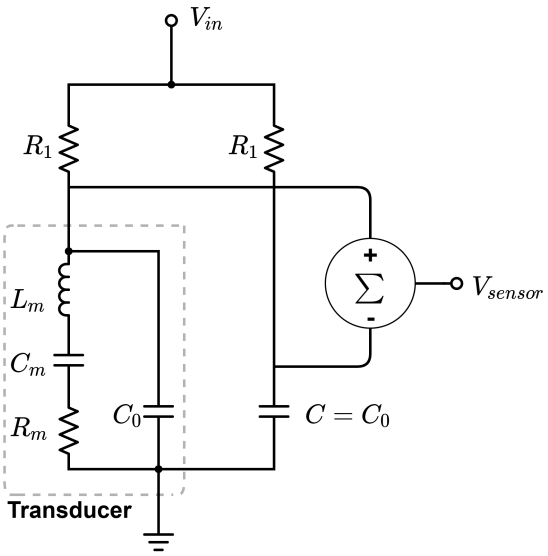

Figure 2.15: Transducer vibration sensor from [37]. The sensor voltage is proportional to the transducer velocity when C approximates C_0 of the transducer.

damping over a broad frequency range. A problem is that this implementation requires a capacitor C which must match very accurately to the transducer capacitance C_o for the sensor to work properly.

2.5 Summary

The most practical form of Q-factor control for an ultrasound transducer is by placement of a shunt, which in its most basic form is a single resistor. A method will have to be devised to determine the optimal shunt value, as well as determining whether additional shunt components can reduce damping further. Because there is an optimum shunt value, an issue with shunt damping is that there is a theoretical limit to the maximum damping it can achieve. Another way of damping transducer oscillation is by modifying the driving waveform, however it seems likely that small inaccuracies in either the driver or the transducer can reduce efficacy greatly. Furthermore current research on this is only empirical and doesn't bear much theoretical foundation. Damping via negative feedback may be able to overcome the issues in other damping methods. Firstly unlike shunt damping it does not have a theoretical damping limit, as feedback factor A in figure 2.14 does not have a theoretical upper limit. Furthermore it may prove more manageable and stable than modified driving waveform damping. An issue with its current implementations is that they require significantly more space per transducer as compared to the other two presented damping techniques. A system should be designed implementing the vibration sensor from figure 2.15 in a feedback driver, and a way should be found to limit the amount of components necessary per transducer.

Chapter 3

Damping method design

This chapter will aim to optimize damping methods discussed in section 2.4 for implementation in a real circuit. As discussed in section 2.3, in order to properly design the damping circuits it is first necessary to model the used piezo-electric transducer. Thus this chapter will begin in section 3.1 with the derivation of equivalent model parameters for a selected piezo-electric transducer, based on impedance analysis over a wide frequency range. Then section 3.2 will use this model to design and optimize circuits for a selection of damping techniques.

3.1 Equivalent model parametrization

Equivalent model parameters can be calculated based on material properties and transducer geometry only, without requiring any type of measurement [15]. However to be sure of an accurate representation it was decided to measure the transducer impedance over a wide frequency range, and base the equivalent model parameters on the measurement results. Measurements will be done for two sizes of PZT-5A ultrasound thickness mode transducers: 2x2mm and 4x4mm, both 1mm in thickness. These flat, thickness mode transducers were chosen because of ease of fabrication and handleability. The main interest is the damping of the primary resonant frequency, so it is justified to use the extended BVD model of figure 2.12. Furthermore the measurements will be done on a transducer in air, not mounted on any type of material. The equivalent electrical resistor for an infinite medium of air can be calculated following equation 2.18. For a speed of sound in air $c = 343m/s$, an air density $\rho = 1.3kg/m^3$ and a contact area of $A = 4mm * 4mm = 16 * 10^{-6}m^2$ this yields a resistor value of

$$R_{air} = c * \rho * A = 343 * 1.3 * 0.004^2 = 7m\Omega \tag{3.1}$$

Because of the low surface area of the transducer, the air resistance is very low and the behaviour around the primary resonant frequency can be approximated by the behaviour in free space, which is simulated by the standard BVD model shown in figure 2.10B.
Based on equation 2.8 the transducer impedance takes the shape of the graph shown in figure 3.1. The standard BVD model has a single resonant frequency f_r and anti-resonant frequency f_{ar}. Based on the value of f_r and f_{ar}, as well as the impedance Z_r and Z_{ar} at these frequencies, the component values of the BVD-model can be derived.

3.1.1 Method

In order to calculate the BVD-model component values of a transducer of interest, first its impedance and phase response must be measured using an impedance analyzer. Then, component values can be approximated using the following set of formulas [39]:

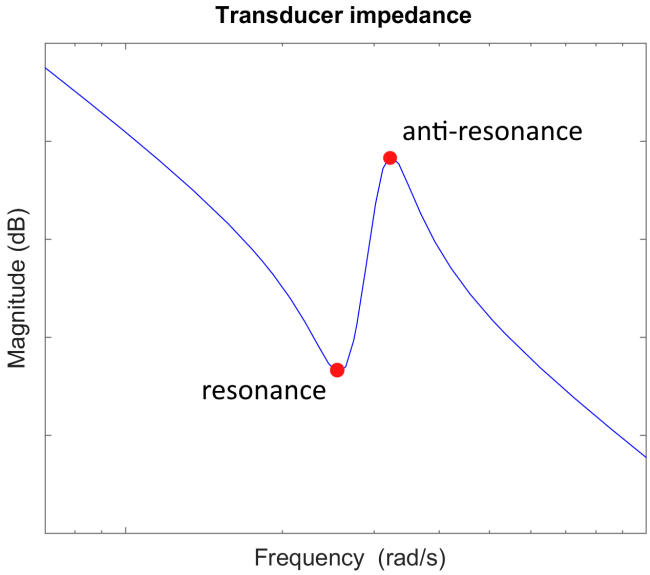

Figure 3.1: Transducer impedance curve based on the BVD-model. The resonant and anti-resonant frequencies are assumed to be at the local minimum and maximum respectively.

$$C_o = \frac{-Im(Z_r)}{2\pi f_r |Z_r|^2} \tag{3.2}$$

$$R_m = \frac{|Z_r|^2}{Re(Z_r)} \tag{3.3}$$

$$C_m = C_o \left[\left(\frac{f_{ar}}{f_r} \right)^2 - 1 \right] \tag{3.4}$$

$$L_m = \frac{1}{(2\pi f_r)^2 C_m} \tag{3.5}$$

Here $Re(Z)$ and $Im(Z)$ are the real and imaginary parts of the impedance following

$$Re(Z) = cos(\phi)|Z| \tag{3.6}$$

and

$$Im(Z) = sin(\phi)|Z| \tag{3.7}$$

where ϕ is the phase response at a certain frequency. After making the initial component approximations, the resulting impedance curve can be curve fitted to the measurement to improve accuracy. Because the capacitor values will be small in a numerical sense, it is difficult curve fit to their absolute value. For this reason coefficients k_o and k_m are used for C_o and C_m respectively, as suggested by [40]. Based on equation 2.8, this results in the following model

$$\frac{s^2 k_m C_m L_m + s k_m C_m R_m + 1}{s^3 k_o C_o k_m C_m L_m + s^2 k_o C_o k_m C_m R_m + s(k_o C_o + k_m C_m)} \tag{3.8}$$

with C_m and C_o as constant values set by equation 3.4 and equation 3.2, and k_o, k_m, L_m, R_m as parameters. The initial parameter values will be 1 for k_o and k_m, and the results of equation 3.3 and equation 3.5 for R_m and L_m. For the curve fitting algorithm, the Matlab trust-region-reflective algorithm will be used. The developed Matlab code can be found on Github [41].

3.1.2 Measurement setup and preparation

For the impedance measurements a Keysight Impedance Analyzer E4990A 20Hz-120MHz is used. A tungsten wire will be attached to either side of the transducer, in order to be able to connect it to the impedance analyzer. The wires must be kept short as to minimize parasitic resistance and inductance. The tungsten wires were attached to the transducer one by one using ThermoScientific silver conductive adhesive paste. First, the transducer is placed upon a heating plate. Then, the tungsten wire is placed on top of the transducer and a small drop of conductive silver paste is added on top, connecting the wire and transducer. Finally, the heating plate is set to a temperature of $93°C$ and the silver paste is cured for 15 minutes. Once one side is cured, the transducer is flipped and the process is repeated for the other side.
In conjunction with the impedance analyzer, a Keysight 16047E test fixture was used to clamp the transducer wires. Before starting the impedance measurements, the impedance analyzer was calibrated for the test fixture. After calibration, the wires can be clamped. A frequency sweep was done from 200kHz to 3MHz.

3.1.3 Results

Measurements were done for the two sizes of PZT-5A ultrasound transducers: 2x2mm and 4x4mm. For each size, four different transducers were measured independently. The measurement results are shown in figure 3.2. A big discrepancy in primary resonant frequency is observed between the two sizes

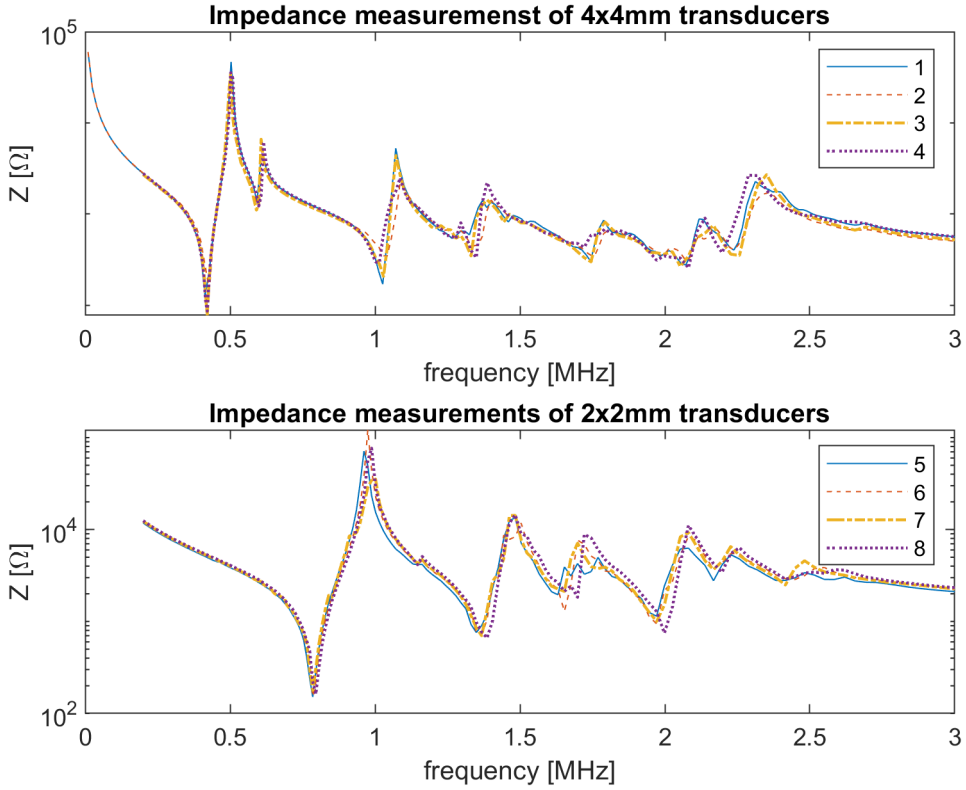

Figure 3.2: Impedance magnitude plots of four 4x4mm (top) and 2x2mm (bottom) PZT transducers.

of PZT, 420kHz for the 4x4mm and 785kHz for the 2x2mm transducer. This is in accordance with previous studies showing that the center frequency increases with reducing surface area for thickness mode transducers [16]. As this thesis does not necessarily require very high frequency ultrasound, the

4x4mm transducer was chosen to be used in the rest of this thesis because it is easier to handle by hand.
Calculation and curve fitting was done as described in section 3.1.1. Curve fits for the primary and a secondary resonant frequency of a 4x4mm sample are shown in figure 3.3. The corresponding component values can be found in table 3.1. Note that as should be expected, the values of C_o are very similar.

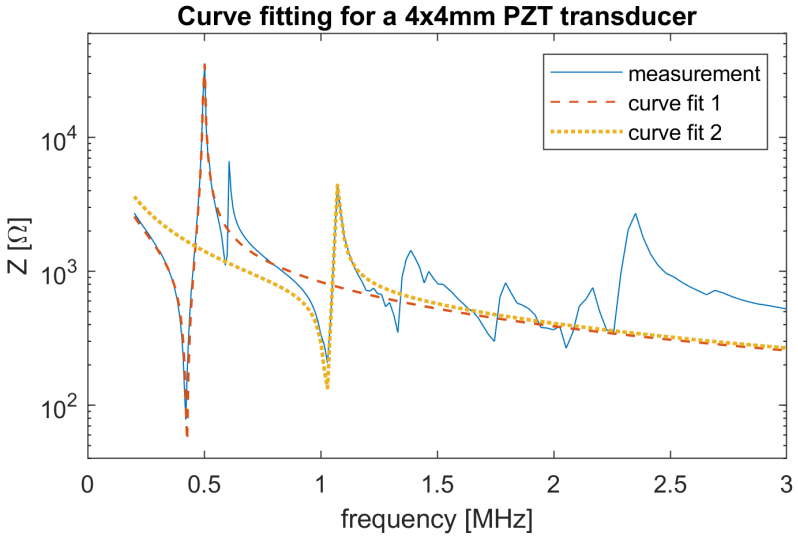

Figure 3.3: Measurement of a 4x4mm PZT transducer accompanied by curve fits of two resonant frequencies.

primary f_r

Component	Value
C_o	209pF
C_m	79.3pF
L_m	1.76mH
R_m	42Ω

secondary f_{r2}

Component	Value
C_o	201pF
C_m	18.1pF
L_m	1.33mH
R_m	125Ω

Table 3.1: BVD model component values of a 4x4mm PZT transducer

3.2 Damping optimization

Equipped with the proper knowledge on ultrasound transducers, previously proposed damping methods and how to model them, it is now possible to create new optimized designs for electronic Q-factor control. First transducer driving by modified waveform will be analyzed using one of the simplest most effective excitation waves demonstrated by Persson et al. [35], which can be referred to as a 'counterpulse'. Then, shunt damping will be analyzed and optimized in terms of efficacy and used area. Finally, a novel feedback Q-factor control method is proposed based on the vibration sensor of figure 2.15, which is able to overcome the challenge of used area per transducer when applied to transducer arrays.

3.2.1 Counterpulse system

The simplest and one of the most effective excitation waves demonstrated by [35] is a square pulse with a duration equal to a full period of the transducer resonant frequency. This will be referred to as a counterpulse, as it counters the continued vibration of the transducer. In this case first a voltage is applied to kick-start the transducer oscillation at its natural frequency. Then, the signal will return the input to ground after one full oscillation. This way, after one cycle, the step response will be summed with the negative step response, optimally cancelling out any vibration in the transducer. In figure 3.4A, the response of a transducer in free space is shown without a counterpulse. Then in figure 3.4B an example of the counterpulse is shown. A drawback of this method is the complete reliance upon the exact duration of the pulse in relation to the response of the transducer. As seen in figure 3.4C a small inaccuracy can cause a significantly reduced efficacy. Another drawback is that this method will

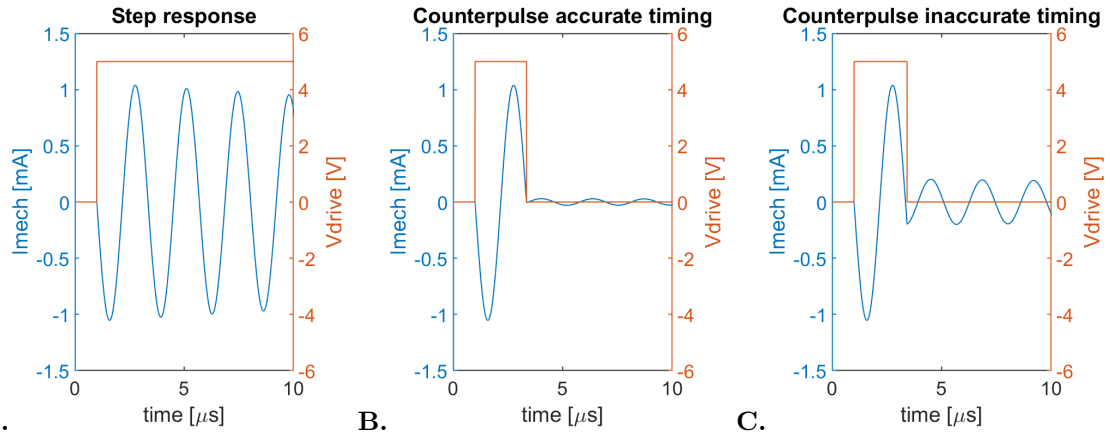

Figure 3.4: **A.**: Applying a step function voltage to a transducer in free space causes a high Q-factor oscillation. **B.**: Further oscillations in i_{mech} are highly attenuated by driving the transducer with a pulse with a duration of exactly T_0. Some oscillation still remains because of the transducer's intrinsic Q-factor: the oscillatory energy has already decreased by the end of the pulse and therefore the anti-phase oscillation is larger than the original oscillation. **C.**: A small shift in the transducer resonant frequency causes increased residual amplitude.

work less well on a transducer with an already low Q-factor, as the counterpulse will then cause an over-correction. For perfect execution two things are necessary: first of all to know the exact resonant frequency of the transducer, and secondly, precise timing of the switch. Piezo-electric transducer elements are fabricated to resonate at a specific frequency, so this frequency is known beforehand. One problem is that environmental influences can impact the resonant frequency. Changes in temperature can cause the resonant frequency to shift by a few percent [42]. Figure 3.4B shows that a shift in resonant frequency of only a few percent can significantly impact the performance. To get rid of

this problem an adaptive system is needed which allows for variable pulse width depending on either temperature sensor readings or direct measurements of the resonant frequency. This will however highly increase system complexity. Another solution is to combine the counterpulse method with other damping methods, such as shunt damping.

3.2.2 Shunt damping

Section 2.4.1 shows that shunt damping can reduce the Q-factor of a transducer. Shunt damping is a good candidate for Q-factor control as it is a simple method that doesn't take up much space; A single resistor per transducer can suffice. This section will investigate how to optimize the value of the shunt and how to implement it in a circuit.
When setting the shunt Z_{shunt} in figure 2.13 to a single resistor R_a, the voltage over transducer $X1$ is defined as

$$V_{X1} = \frac{Z_{X1}}{R_a + Z_{X1}} V_{in} \tag{3.9}$$

Using the BVD-model definition of mechanical current i_{mech} in equation 2.9, when substituting E with equation 3.9 it follows that

$$\begin{aligned} i_{mech} = \frac{sC_m}{s^3 R_a C_o C_m L_m + s^2 C_m (L_m + R_a R_m C_o)} V_{in} \\ + s(R_m C_m + R_a(C_o + C_m)) + 1 \end{aligned} \tag{3.10}$$

Varying the value of R_a will influence the properties of i_{mech}, thus also the Q-factor. However, determining the Q-factor from the transfer function is no longer as mathematically straightforward as it was for the undamped transducer, as the mechanical current is now a third order system. Making R_a very low or very high will yield high peak in the current at the resonant or anti-resonant frequency of the transducer respectively.The approximate optimal value of R_a is where the center frequency of i_{mech} is shifted right in between the resonance and anti-resonance frequency of the piezo-electric transducer [18]. The optimal value for R_a is thereby approximated by equation 3.11 [18].

$$R_a \approx 2\sqrt{\frac{L_m C_m}{C_o(4C_o + C_m)}} \tag{3.11}$$

Inserting the component values from table 3.1 into equation 3.11 the resulting theoretical optimum is at $R_a = 1.7k\Omega$. To verify this, the transfer function for i_{mech} equation 3.10 was simulated in Matlab for varying R_a in a range around the theoretical optimal value. For every value of R_a the Q-factor was calculated according to $Q = f_c/B$, where center frequency f_c is where the frequency response peaks, and B is the bandwidth in Hz. Figure 3.5 plots the Q-factor of i_{mech} against R_a. It can be seen that the optimal R_a is about $1.4k\Omega$ for this transducer. The Q-factor quickly rises as R_a becomes too low, while taking R_a too high still results in a good quality factor. In conclusion equation 3.11 gives a good indication of the optimal value for R_a. Then, the Q-factor can be plotted against R_a in the neighbourhood of the initial result to find the true optimum. The same paper shows that adding an inductor in series with the shunt resistor can improve the damping even further, with an optimum value approximated by equation 3.13 [18]. This yields a value of $639\mu H$. With $Z_{shunt} = R_a + sL_a$, the mechanical current is defined as

$$\begin{aligned} i_{mech} = \frac{sC_m}{s^4 C_o C_m L_a L_m + s^3 R_a C_o C_m L_m} V_{in} \\ + s^2(C_m L_m + L_a[C_o + C_m]) \\ + sR_a(C_o + C_m) + 1 \end{aligned} \tag{3.12}$$

and

$$L_a \approx R_a\sqrt{L_m C_m} = \frac{R_a}{\omega_0} \tag{3.13}$$

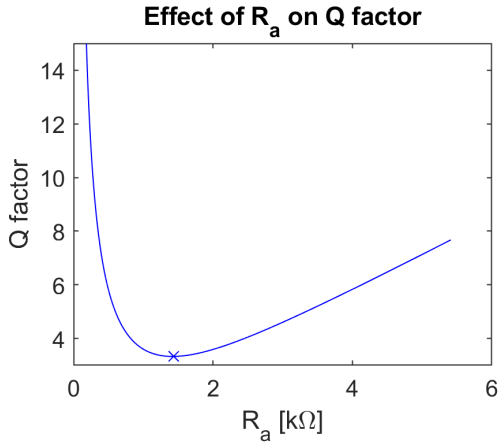

Figure 3.5: Mechanical quality factor vs. shunt resistor R_a. $R_a = 1.4k\Omega$ yields the lowest Q-factor.

To verify this, the Q-factor was plotted against a varying L_a, for different values of R_a as seen in figure 3.6. It can be seen that lower values of R_a yield strange results. This is because as shunt values stray too far from the optimum, two resonant peaks are introduced - as can be seen in figure 3.7 -, which renders the Q-factor a dubious figure of merit. It must be noted as well that the optimal value for L_a

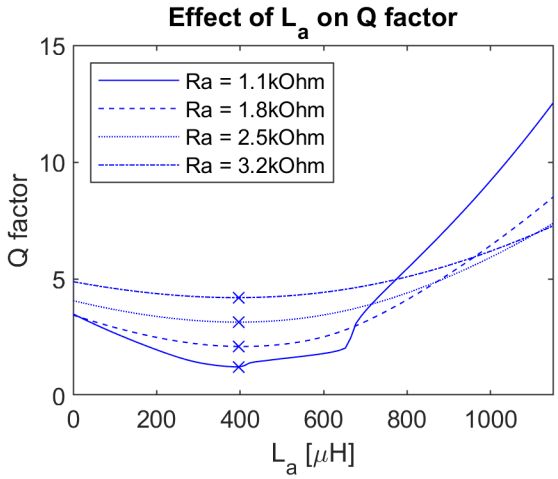

Figure 3.6: Value of inductor L_a vs resulting Q-factor for different values of resistor R_a. The optimal L_a can be seen to be independent of R_a.

does not depend on R_a nearly as much as equation 3.13 suggests. In fact for all plotted curves the optimal L_a is $396\mu H$. Now that an inductor is added, the optimal value of R_a may have changed as compared to R-damping, and should therefore be optimized again. Taking $L_a = 396\mu H$, the frequency response of the system can now be plotted for different values of R_a , see figure 3.7A. Note that for R_a too high the damping is reduced, while for R_a too low i_{mech} contains two resonant peaks. The optimum can be found systematically by observing that the resonant frequency is constant for R_a too high. The point of best damping is thus found by finding the value where the peak gain frequency dips below the resonant frequency found in R-damping. This also corresponds with the point where the peak gain begins to rapidly increase as is shown in figure 3.7B. The optimum is around $1.1k\Omega$. The Matlab script developed to automate the process of finding the optimal values for R_a and L_a for both R-damping and RL-damping is found on Github [41].

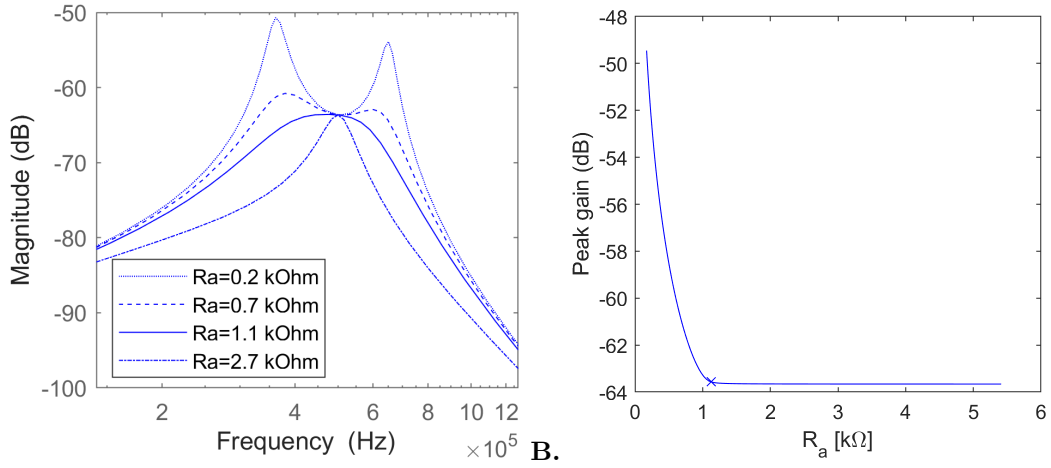

A. **B.**

Figure 3.7: **A.**: Frequency response for different R_a in RL-damping circuit. **B.**: Peak gain for different R_a. The optimum is found at $R_a = 1.1k\Omega$.

Figure 3.8 summarizes the transducer response in an undamped situation versus optimized R- and RL-damping. It can be seen clearly how the bandwidth is increased significantly with both shunt variations.

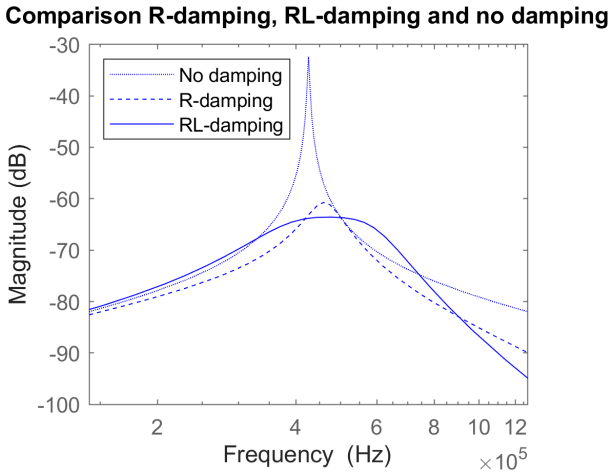

Figure 3.8: Comparison of undamped, R-damped, and RL-damped transducer frequency response

Replacing the inductor

Inductors are large components with many undesirable traits and thus it is desirable to replace them with components such as resistors, capacitors and op-amps for easier implementation in integrated circuits. A simple inductor simulating circuit can be built using a single opamp, shown in figure 3.9. First, the input impedance will be analyzed by assuming an ideal opamp. From the assumption of the ideal opamp it follows that $i_{in} = i_{R_a} + i_{R_b}$. Furthermore $i_{R_a} = \frac{V_{in} - V_{R_b}}{R_a}$ and $i_{R_b} = \frac{V_{R_b}}{R_b}$. Now inserting $V_{R_b} = V_{in}\frac{R_b}{R_b + Z_{C_b}} = V_{in}\frac{sR_bC_b}{1+sR_bC_b}$ into the equations for i_{R_a} and i_{R_b} yields the following expression for

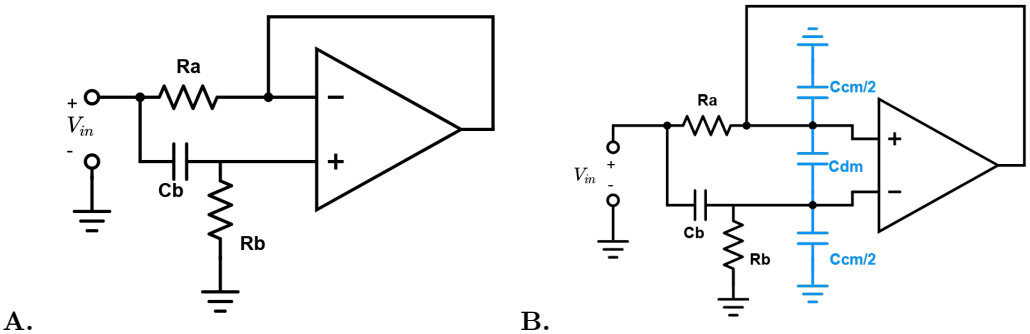

A. **B.**

Figure 3.9: **A**.: Simple inductor simulator circuit using a single opamp. **B**.: Inductor simulator with added non-idealities C_{dm} and C_{cm}.

i_{in}:

$$i_{in} = V_{in}(\frac{1}{R_a + sR_aR_bC_b} + \frac{sC_b}{1 + sR_bC_b}) \tag{3.14}$$

$$= V_{in}\frac{1 + sR_aC_b}{R_a + sR_aR_bC_b} \tag{3.15}$$

Thus Z_{in} is given by equation 3.16:

$$Z_{in} = \frac{R_a + sR_aR_bC_b}{1 + sR_aC_b}[\Omega] \tag{3.16}$$

As long as the product of R_a and C_b is negligible, Z_{in} can be approximated by

$$Z_{in} \approx R_a + sR_aR_bC_b \tag{3.17}$$

This represents a resistor R_a in series with an inductor

$$L_a \approx R_aR_bC_b[H] \tag{3.18}$$

The values of R_a and L_a can be determined by the matlab script described before. By setting a constraint on the significance of sR_aC_b the value of C_b can be determined. This can be stated more generally by saying

$$C_b << \frac{1}{\omega_0 R_a} \tag{3.19}$$

The optimal value for L_a then determines the value of R_b.
When considering a real opamp implementation, it must be considered what happens when C_b gets very low. Non-ideal opamps have a differential and common mode capacitance, C_{dm} and C_{cm}, which can interfere with the circuit functionality. These are shown in figure 3.9B. When C_b starts to approach the range of the opamp input capacitances, they will start to have a significant impact on Z_{in}. Any deviation from the optimal Z_{in} means the damping efficacy is reduced. Therefore another constraint can be denoted for C_b as:

$$C_b >> C_{in} \tag{3.20}$$

Where C_{in} refers to both C_{dm} and C_{cm}. And so

$$C_{in} << C_b << \frac{1}{\omega_0 R_a} \tag{3.21}$$

Thus follows a working range for C_b. Filling in the values for ω_0 and R_a this gives

$$C_b << \frac{1}{2\pi * 426kHz * 1126\Omega} = 332pF \tag{3.22}$$

Furthermore an opamp must also be chosen so that its input capacitance is low enough, as limited by this same equation 3.21.

3.2.3 Proposed feedback Q-control method

As discussed in section 2.4.3, it has been shown that feedback circuits can be used to lower the Q-factor of piezo-electric transducers. A problem not mentioned is the fact that building a separate feedback circuit around every element in a transducer array will take up way too much circuit area to be practically applicable. This section proposes a novel solution that uses only a single feedback circuit around one "dummy" transducer to drive multiple transducers in an array. It applies the vibration sensor figure 2.15 in an amplifier and negative feedback loop. Then, the idea is exploited that the voltage over impedance bridge can simply be buffered onto other transducers to provide the same damping. Basically this way a self regulating modified waveform driver is created. Proving its efficacy would mean an electronic damping design is created which can be plugged into many different ultrasound transducer array designs and easily extendable to a large amount of transducers.

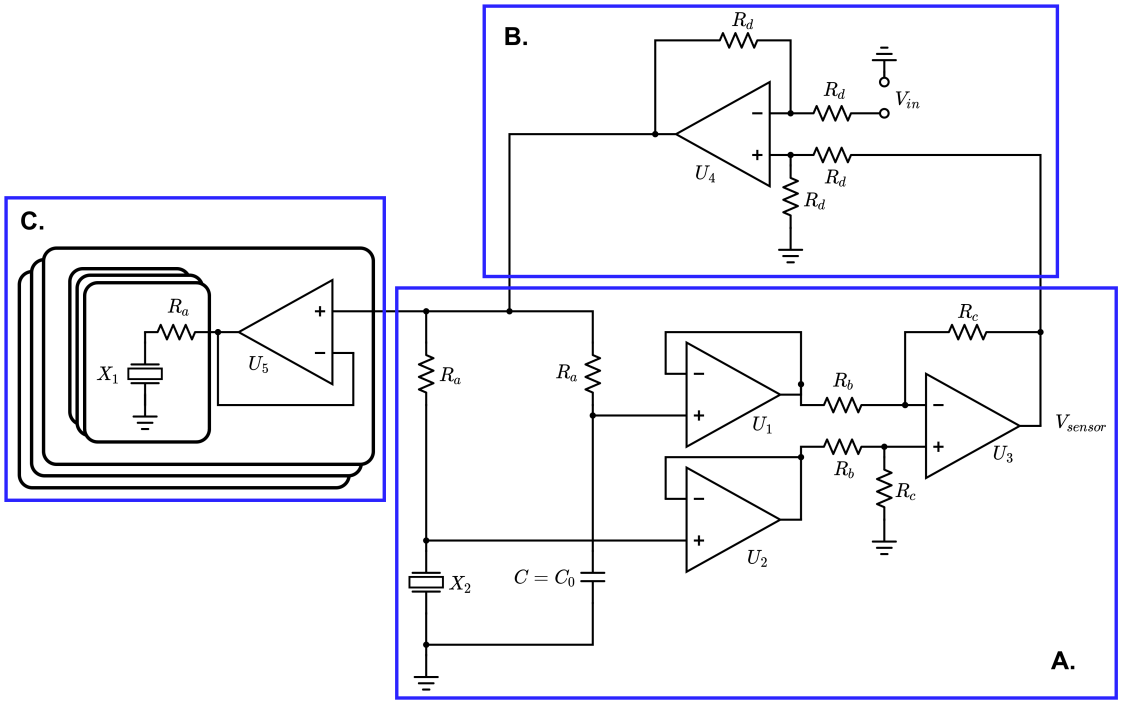

Figure 3.10: Feedback damping circuit using an impedance bridge sensor. **A.** Transducer velocity sensor. V_{sensor} represents the velocity of transducer X_2. **B.** U_4 combines input voltage V_{in} and the sensor voltage V_{sensor} to provide negative feedback into the impedance bridge. **C.** Buffer U_5 aims to set a voltage over transducer X_1 as that over transducer X_2. The buffer can be connected to several resistor-transducer pairs, as long as it can provide enough current. Furthermore the entire block C can be repeated to facilitate driving many transducers.

Figure 3.10A shows an implementation of the sensor from figure 2.15 which already has an amplification factor built in. Buffers U1 and U2 are used to isolate the impedance bridge from the subtractor U3. The output of U3 follows the equation

$$V_{sensor} = \frac{R_c}{R_b}(V_{X2} - V_C) \tag{3.23}$$

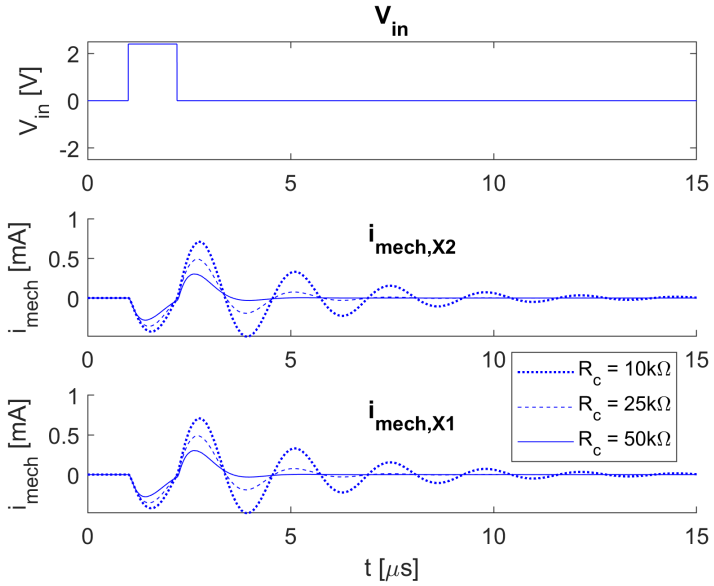

Figure 3.11: Results of LTSpice simulation of the feedback circuit in figure 3.10. The circuit is driven by a single pulse at resonant frequency (V_{in}). $i_{mech,X2}$ and $i_{mech,X1}$ show the mechanical current through the BVD-model RLC-branch of transducers X2 and X1 respectively. By increasing R_c, damping is improved at the cost of signal amplitude.

Assuming a BVD transducer electrical model where capacitance C_0 is in parallel with the mechanical branch Z_{mech} and its mechanical current i_{mech}, representing the transducer velocity, after some algebra the sensor voltage is defined as:

$$V_{sensor} = -\frac{R_a R_c}{R_b} \frac{1}{1 + sR_aC} i_{mech} \tag{3.24}$$

The feedback amplification factor can thus be controlled by varying the ratio of resistors R_c and R_a to R_b. It should be noted as well that resistor R_a forms a lowpass filter with capacitor C. R_a should be chosen such that

$$R_a < \frac{1}{\omega_0 C_0} \tag{3.25}$$

to make sure that the resonant frequency is not attenuated by the filter. Figure 3.10B provides the feedback part of figure 2.14. The amplification factor is in this case integrated in the sensor, while U4 only provides a simple subtraction. Figure 3.10C shows how multiple buffers can be used to drive a multitude of transducers based on one feedback loop. In this schematic, phase delay between transducers cannot be controlled and therefore such a transducer array could only send plane waves. To allow focused ultrasound, phase delay subcircuits should be implemented in block C.
The feedback driver was simulated in LTSpice using the BVD-model for transducers X2 and X1, using the values of table 3.1. Capacitor C is set equal to C_0 of the transducers. To obey equation 3.25, R_a was chosen as 100Ω so that with $C = 209pF$, the cutoff frequency of the lowpass filter formed by R_a and C is equal to

$$f_c = \frac{1}{2\pi * 100\Omega * 209pF} = 7.7MHz \tag{3.26}$$

which is much higher than the resonant frequency of the transducer. Other resistors are defined as $R_b = 1k\Omega$, and $R_d = 10k\Omega$. Results are compared for $R_c = 10k\Omega$, $25k\Omega$ and $50k\Omega$. For the opamps an ideal opamp was used. The simulation result is shown in figure 3.11. It can be seen that the vibration in both transducers is identical, and that it dies out rapidly for both. However for increased damping performance, the signal amplitude is reduced.

3.3 Summary

In summary, transducer driving by counterpulse can in theory produce great damping but it shows that a small inaccuracy can greatly reduce efficacy. Implementation in practice should show whether or not it can be effective. A way for systematic determination of the optimal shunt values was devised and executed for the measured transducer equivalent model component values. These shunts including the RL-simulator will be built on the PCB for verification. A drawback of shunt damping is that it can not provide any more damping beyond the optimum point, so there is a limit to the minimum Q-factor it can achieve for a given transducer. The proposed Q-factor control circuit does not have this issue as the gain factor in figure 3.10A does not have a theoretical limit. Furthermore as can be seen in figure 3.10C the feedback circuit actually requires less components per transducer than the RL-simulator of figure 3.9A when applied to an array of transducers. Lastly it can be said the proposed feedback circuit is more easily adaptable to various transducer arrays, as the only component that has to be taylored specifically to the used transducer is capacitor C which should be equal to C_0 of the transducer. This may in future applications even be done with a switched capacitor bank, allowing for precise control of the C value. The proposed feedback Q-factor control circuit will be tested for one dummy transducer X_2, and provide damping to a single output transducer X_1, which will be the same transducer as used for the other damping methods.

Chapter 4

System development

4.1 System design

In section 3.2 damping techniques for piezo-electric transducers were identified and optimized. This section will cover the design and implementation of a PCB supporting these proposed methods for electronic Q-factor control. By combining them on a single PCB, the damping techniques can be verified and compared against each other and infer the benefits of the proposed Feedback Q-control method, providing a solid foundation to make recommendations for future work.
To perform measurements on the PZT, the system shown in figure 4.1 will be used. The PZT is placed within a small water container on the board, as to simulate its behaviour on human tissue. The vibrations produced by the transducer will be measured by a hydrophone submerged in water. This data is visualized on an oscilloscope and can be saved on a computer or USB. The PZT will be driven using the damping techniques described in the previous chapter, which will be built on the PCB. The circuit will be controlled by an FPGA and is powered by an external power supply.

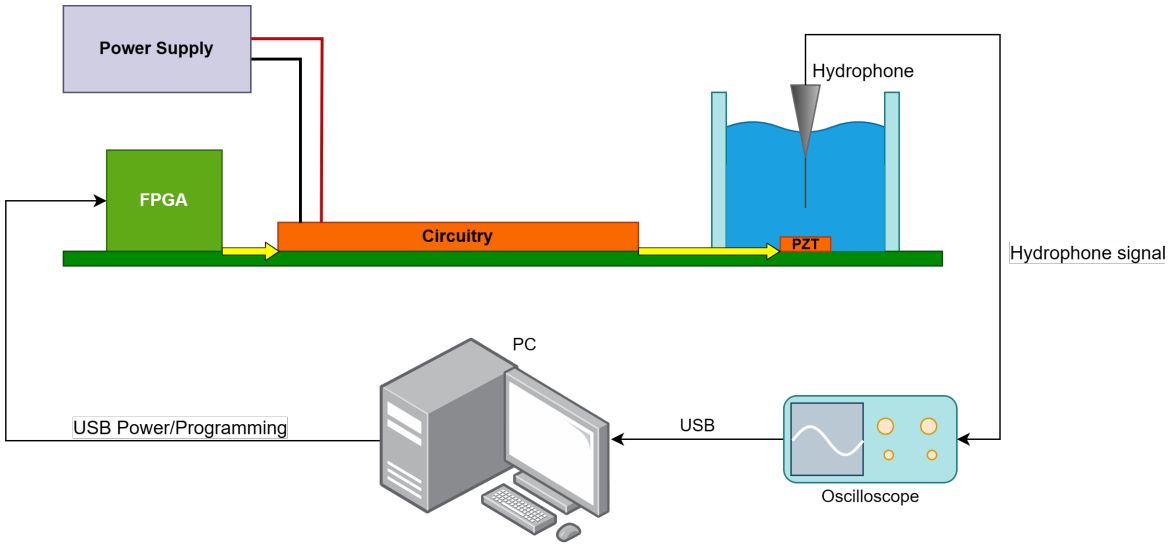

Figure 4.1: An overview of all major system components. An FPGA is programmed and powered by a PC. The FPGA sends control signals to the circuitry on the PCB which is powered by a single ended power supply. The PCB circuitry provides a driving signal for the PZT transducer in the water tank. The signal produced by the PZT is picked up by the hydrophone and visualized on an oscilloscope. The recording can then be transferred to the PC through a USB-stick.

The used damping techniques are:

- Shunt damping (R/RL/RL-simulator)
- Proposed Feedback Q-control method
- Counterpulse (solo/with shunt/with feedback method)

The board must be able to:

- Drive a single PZT element mounted on the PCB with arbitrary digital waveforms provided by the FPGA near the resonant frequency of 420kHz.
- Switch freely between the different damping methods through control signals provided by the FPGA.
- Be powered by one single-ended power supply source. The FPGA can be powered seperately via USB.

From above requirements a preliminary overview of the circuit's subsystems can be made:

- Power supply unit
- Shunt selector (selects one of the different shunts)
- Feedback driver
- Transducer Driver
- Source selector (controls which damping method is used)

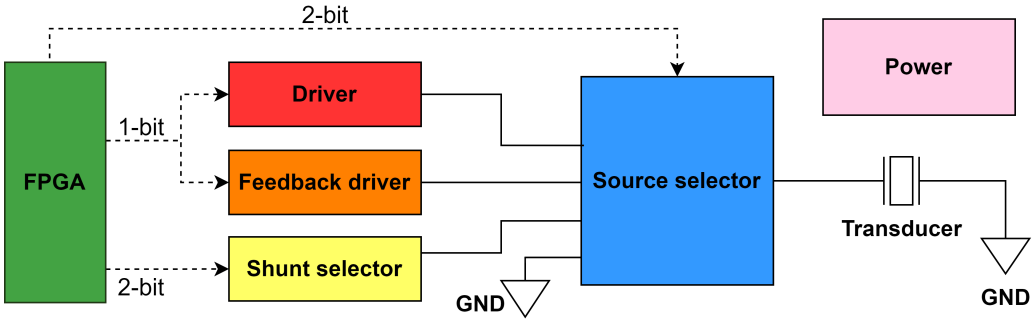

Figure 4.2: Block diagram of the electronic circuit for Q-factor control. The transducer on the right can be connected to different blocks via the source selector (blue). The driver (red) and feedback driver (orange) are controlled by a binary input signal. The driver outputs a binary signal to drive the transducer. The feedback driver will output a complex voltage waveform based on a negative feedback circuit around a dummy transducer, to dampen the vibration of the main transducer. The shunt selector (yellow) should be able to select up to four different shunts to be connected to the transducer based on a 2-bit input signal. As a fourth input to the source selector, the transducer can also be short-circuited to ground (GND). The power block (pink) will convert an external input voltage to voltage levels needed for the other blocks (connections not shown). The FPGA (green) provides all controll signals to the different blocks.

The subsystems are combined in a block diagram shown in figure 4.2. Three functional blocks can be connected to the transducer by the source selector: The driver for modified waveform driving, the feedback driver for applying the proposed feedback Q-control circuit, and the shunt selector for passive transducer damping. The shunt selector is able to select the different shunts R/RL/RL-simulator. All logic is driven by the FPGA. The circuit is powered by an external power supply.

4.2 System implementation

4.2.1 Circuit implementation

This section will explain how the final PCB for this project was developed. The final result can be seen in figure 4.3. The individual functional blocks of the circuit will be described in the sections below, with the letter between brackets referring to the corresponding letter in figure 4.3. Circuit design was done in Altium Designer. The PCB was printed by Eurocircuits. The Altium circuit designs can be found in Appendix A.

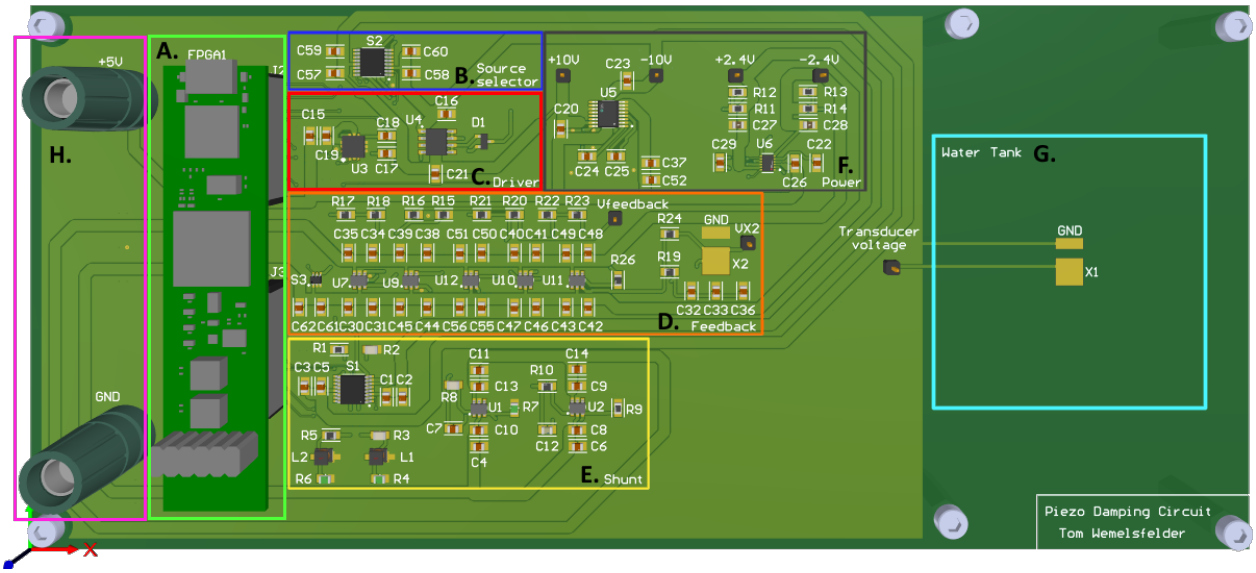

Figure 4.3: Final PCB design in Altium. **A.** Slots for headers to mount the FPGA on. **B.** Source selector. **C.** Driver. **D.** Feedback driver. **E.** Shunt selector. **F.** Power supply unit. **G.** Assigned area for primary transducer and water tank mounting. **H.** Binding posts for external +5V supply and Ground connection.

Shunt selector and shunts (E)

From the opamp constraint in equation 3.22 it is apparent that the used opamps require low input capacitance. The LTC6268 was selected for this particular reason, as it is specifically designed to have ultra-low common mode (450fF) and differential mode (100fF) input capacitance. With a Gain Bandwith Product (GBW) of 500MHz it is able to provide sufficient gain at the operating frequency of $f_r = 420kHz$. The LTC6268 has a supply range limit of 3.1V minimum to 5.25V maximum. Thus a dual supply of about $\pm 2.6V$ is needed for maximum voltage swing.
Based on equations 3.21 and 3.22, capacitor C_b of the inductor simulator circuit in figure 3.9 must now be chosen according to:

$$450fF << C_b << 332pF \tag{4.1}$$

Honoring this limitation, with an R_a of $1.1k\Omega$ as calculated in section 3.2.2, C_b was chosen as $3.6pF$, such that with an R_b of $100k\Omega$ the resulting simulated inductance is equal to

$$L_a = R_a R_b C_b = 1.1k\Omega * 100k\Omega * 3.6pF = 396\mu H \tag{4.2}$$

which is exactly equal to the optimal L_a calculated in section 3.2.2.
Only one shunt should be used at a time and this requires a multiplexer with enough inputs to support

all different shunts. Because an earlier system design was based on more shunts than the three presented here, the DG408DQ-T1 was chosen as it supports eight inputs. It has a reasonably fast transition time of 160ns (order ten faster than the operating frequency). It supports a dual supply of maximum $\pm 20V$.

Source selector (B)

The purpose of the source selector is to allow connecting the transducer in the water tank to one of the following four: Driver, Feedback driver, Shunt selector or Ground. For simplicity, the same multiplexer as for the shunt selector was chosen here.

Driver (C)

For the driver circuit the MD1210K6-G High-Speed Dual MOSFET Driver was used in combination with the TC6320 MOSFET pair as recommended by its datasheet [43]. The output voltage must not exceed the supply voltage of the source selector, therefore the driver circuit will use the same dual supply as the source selector and shunt selector.

Feedback driver (D)

For the same reasons as for the shunts, the opamp of choice for the feedback driver is the LTC6268. This means the driving voltage of the feedback driver is limited by the supply range of the LTC6268, which is at maximum a dual supply of $\pm 2.625V$.
The capacitor in the impedance bridge of figure 3.10 should be equal to the measured C_0 of the transducer, which is $209pF$. However when testing it was found that the capacitance had to be reduced to a value of $110pF$ for optimal performance. Most likely this is because of the influence of parasitic capacitances in the circuit. Resistor R_a was kept relatively low at a value of 100Ω, based on equation 3.26. The ratio of R_c to R_b in the feedback circuit further determines the feedback amplification factor. A large ratio will increase the feedback amplification and therefore improve the damping effect. However for an amplification factor too large it was found the feedback circuit will start clipping. This means the sensor voltage V_{sensor} should not reach the supply voltage level. After testing resistor values of $R_c = 4.75k\Omega$ and $R_b = 715\Omega$, for a voltage gain of $\frac{4750}{715} = 6.64$, were found to achieve the highest level of feedback without clipping. In combination with R_a, this provides a i_{mech} to V_{sensor} amplification factor of approximately $100 * \frac{4750}{715} = 664[V/A]$. Resistors R_d provide no amplification but are only used in a subtractor configuration. For this application resistors of $10k\Omega$ were used.

Power (F, H)

For the opamps and the driver two seperate differential voltages are needed, based on the component datasheets:

- $\pm$1.55-2.625V
- $\pm$5-20V

The differential voltages will be created from a single 5V supply. A MAX864EEE+T integrated circuit (IC) was used to create a dual $\pm 10V$ supply for the driver and multiplexers. For the opamps a LM27762DSSR IC was used to get a dual $\pm 2.4V$ supply from a 5V input.
When testing the circuit, it was found that the 10V differential supply circuitry was not meant for such a driving application and the $\pm$10V could not be reached when the driver was in use. Therefore this part of the circuit was removed and replaced with an external $\pm$10V differential supply.
For the 2.4V supply another problem arose. It turned out the positive and negative supply voltages in the used LTC6268 footprint were swapped around, therefore the 2.4V differential supply chip could not be used in this configuration. Luckily, the only other component using this supply voltage was the

switch at the input of the feedback driver. The switch was removed and piece of tungsten wire was soldered directly from the FPGA driver signal to the feedback circuit input in order to bypass it. The 2.4V supply circuitry was also removed and replaced by an external supply. The positive and negative 2.4V voltage indicators were swapped on the board.

4.2.2 Transducer mounting (D, G)

The 4x4mm PZT transducers were mounted onto the PCB using conductive silver paste, similar to the method described in section 3.1.2. Three connections need to be made for each transducer: transducer onto signal pad, ground wire onto transducer, and ground wire to ground pad.
First, the ground wire was connected to the transducer the same way as in section 3.1.2. After the silver paste was cured, the remaining two connections can be made simultaneously. The PCB is placed upon the heating plate, and a tiny drop of silver paste is placed upon the signal pad. Then, making sure the ground wire is aligned with the ground pad, the transducer is pressed onto the signal pad so the silver paste spreads equally over the transducer face. Finally silver paste is placed onto the ground wire and the ground pad, and the silver paste can be cured. This process is then repeated for the other transducer.

4.2.3 Watertight coating (G)

The transducer, the ground wire and the pads in the tank will be submerged in water. To prevent any short circuits here it is necessary to apply a watertight coating to this part of the circuit. To facilitate this a parylene coating was applied to the watertank area. Parylene coating is applied by introducing it to the board in gaseous form, it then slowly deposits onto the board as a thin, watertight coating. Preferably the coating is only applied where it is needed. Therefore, before applying the coating, the entire PCB with exception of the water tank section was securely sealed, see figure 4.4.

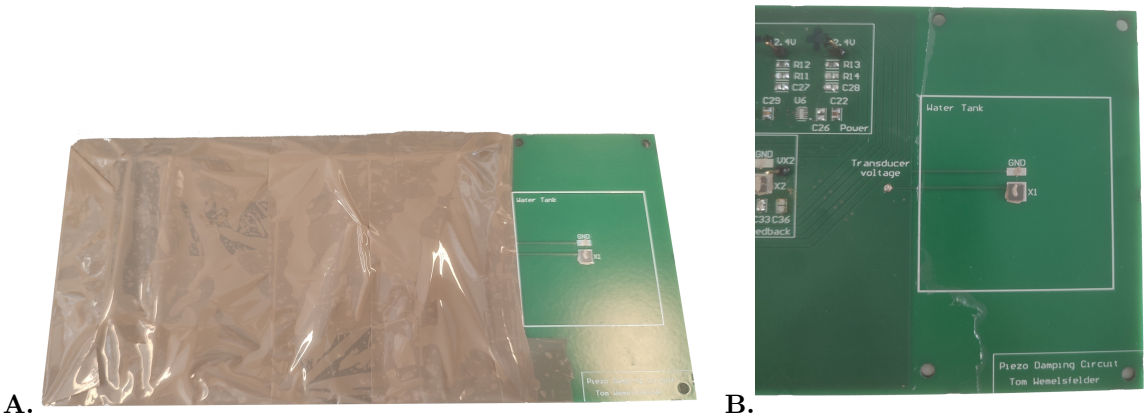

A. **B.**

Figure 4.4: **A.**: Circuitry outside of the watertank is sealed off using a plastic bag and duct-tape. **B.**: Parylene coating result. A thin layer of coating is visible in and around the water tank area. A small breach can be observed within the water tank area. This will be resolved later by placement and sealing of the water tank.

4.2.4 Water tank (G)

The water tank was made from Ultimaker PLA with a 3D printer using Fused Deposition Modeling. Its walls are 5.5cm long, 5cm tall and 0.5cm thick. The water tank was glued onto the PCB using superglue. After the glue dried, all edges were sealed with Bison Super Silicone to prevent any water leakage, as shown in figure 4.5.

A. 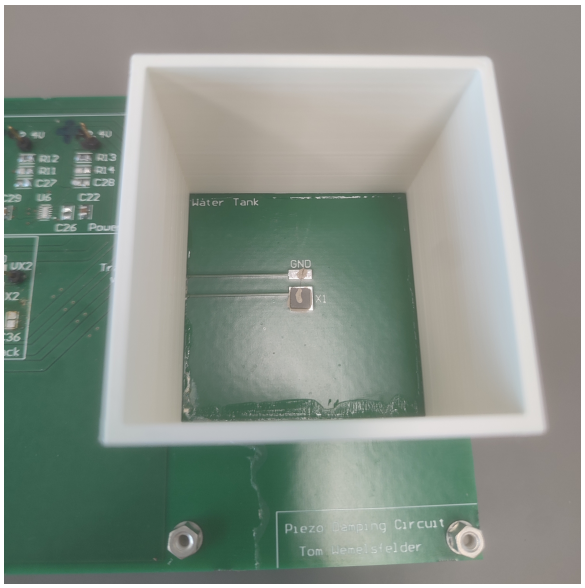

B. 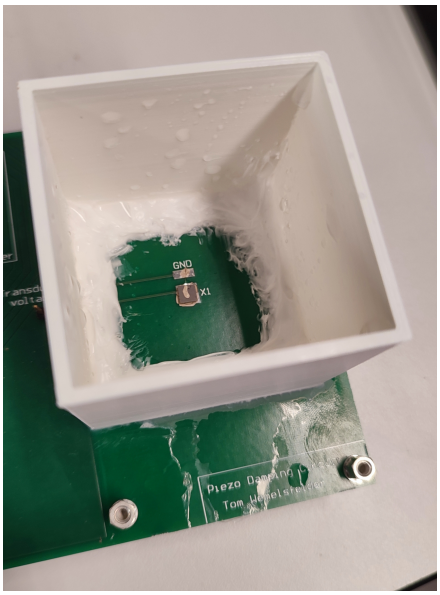

Figure 4.5: Mounting the water tank onto the PCB. **A.**: water tank is glued to the board. **B.**: seams are filled with silicone to prevent water leakage.

4.2.5 FPGA programming (A)

The FPGA used is the CMOD SPARTAN S7. It contains two buttons for simple user control. The FPGA was programmed in such a way that to allow cycling through all desired modes of operation using these two buttons. In this section the VHDL code is explained and visualised using flowcharts. The code itself can be found on Github [41].

Button debouncer

First of all, it has to be made sure the buttons can be used properly. When a button is not pressed, the FPGA will see a steady '0', but when a button is pressed the signal seen by the FPGA will generally not be a steady '1'. Instead it will jitter between both digital values. To prevent registering many button presses a common solution is what is called a button debouncer. An internal "button state" is decoupled from the actual button input signal. When a first '1' is seen on the input, the button state will go to '1' as well. However the button state will only return to '0' once the button input has been '0' for long enough. This is a simple way of filtering out any high frequency jittering. The process is visualised in figure 4.6. The FPGA has two buttons that we will call Button_1 and Button_2. Button_1 will be used for the damping mode controller and Button_2 for the shunt selector. These systems take the corresponding Button_1_TRIG and Button_2_TRIG produced by the button debouncers as input, indicating the moment either button is pressed.

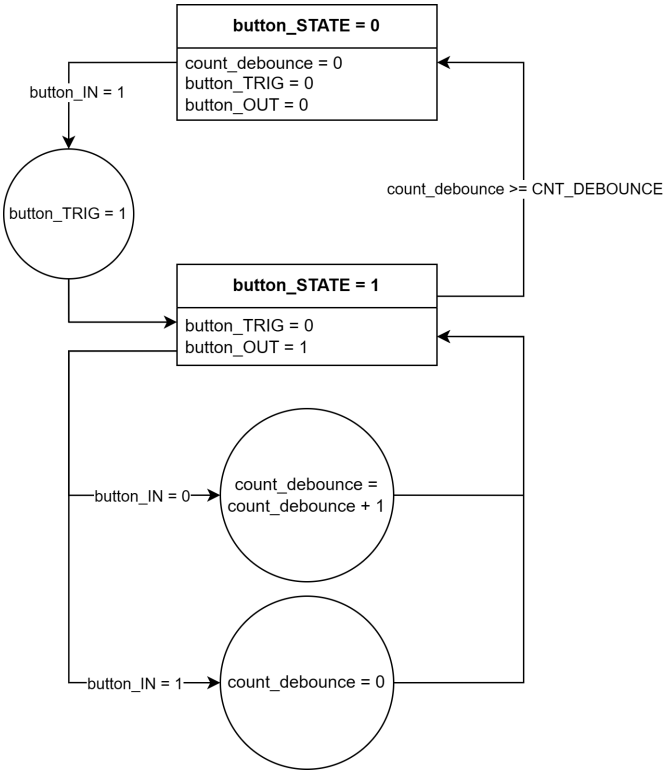

Figure 4.6: Button debouncer flowchart. When a button is 'off' (**button_STATE = 0**), it will turn on immediately after button press is detected. However when the button is 'on' (**button_STATE = 1**) it can only return to the 'off' state after detecting no button press for an extended period of time.

Damping mode controller

The design of the PCB allows us to drive the transducer with arbitrary binary 10V signals, connect different electrical shunts or drive the transducer using the feedback circuit. Firstly, two driving waveforms were selected:

- Single pulse
- Counterpulse

The feedback circuit will use the same waveforms as the driver. Directly after applying one of the waveforms it must be possible to connect the transducer to any of the shunts. With two possible driving waveforms for both the driver and the feedback driver, and including a passive state where no signal is sent, this gives five main control states as depicted in the Finite State Machine (FSM) in figure 4.7. In the Standby phase the transducer will be connected to ground. in the single pulse and counterpulse states, the transducer will be driven by the Driver subcircuit. After excitation, the transducer will be connected to a shunt if one is selected, as will be described in the next figure. The feedback single pulse and feedback counterpulse states make use of the Feedback Driver subcircuit only. Cycling through the states is possible by pressing Button_1 (Button_1_TRIG).

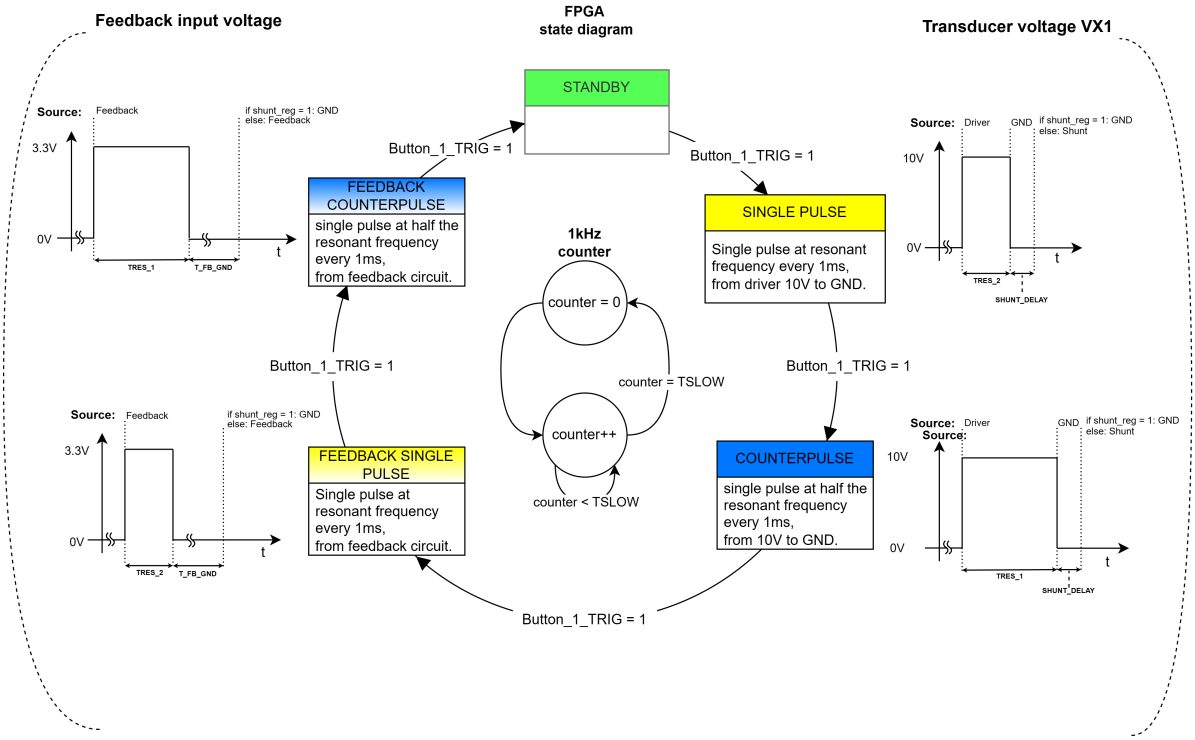

Figure 4.7: Flowchart of the transducer driving states. The right side shows the Single Pulse and Counterpulse states, where the transducer is driven by the 10V driver. There is a short delay before connecting the shunt to let the transducer discharge. The left shows how the same pulses are input for the feedback driver. A standby state is added where the transducer is shorted to ground. In any of the driving states, the pulse is repeated at a frequency of $1kHz$.

Shunt selector

The shunt is selected using a separate control scheme, see figure 4.8. Shunt cycling is done with Button_2 (Button_2_TRIG), changing the registered shunt number, shunt_reg. Shunt_reg values 3 to 8 can be used for selecting a shunt. The numbering is due to circuit layout and port numbering in the multiplexer's datasheet. For the final implementation only shunt_reg values 7, 5 and 4 were used for R, RL and RL-simulator respectively.

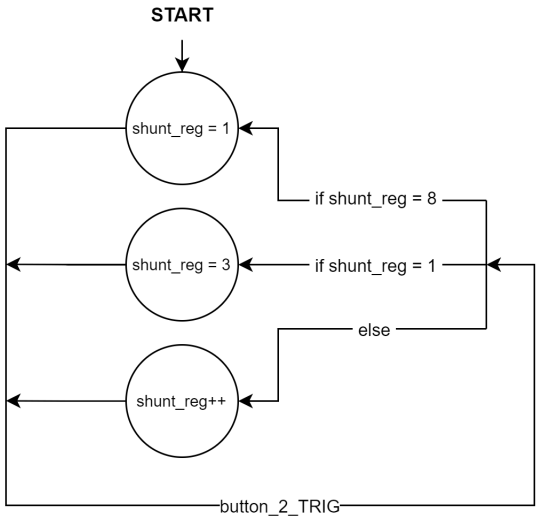

Figure 4.8: Flowchart for the shunt selector. At START, the initial value for shunt_reg is 1. This acts as a flag value for the rest of the VHDL code to signify no shunt should be connected. There is room for selection of six shunts on the board, for this shunt_reg values 3 to 8 are used. Pressing button_2 allows cycling through the shunt_reg values 1 and 3 till 8.

Chapter 5

Results

5.1 Test setup

The test setup was built according to the design in figure 4.1, with the exception of two added differential power supplies for ±10V and ±2.4V in conjunction with a single sided 5V supply. Also, a second probe was added to the transducer voltage V_{X1}, acting as a trigger for the hydrophone measurement. A USB-stick is used to collect the measurement data from the oscilloscope. The oscilloscope was set to average 1024 times and has a sample rate of 2GHz.The water tank was filled with demineralised water. The hydrophone was placed in the water tank as close as possible to the natural focal spot of the transducer. Following equation 2.3, with a resonant frequency f of 420kHz, an element width h of 4mm and speed of sound c in water of $1500m/s$, the natural focal spot is at

$$N = \frac{0.34 * h^2 * f}{c} = \frac{0.34 * 0.004^2 * 426000}{1500} = 1.4mm \tag{5.1}$$

Given the fact that the focal spot is this close to the transducer, the hydrophone was placed a few millimeters from the transducer to avoid risking any contact between them. The hydrophone was moved to hover over different spots along the 4x4mm transducer surface to find the location with the highest signal and the lowest noise. Significant very high frequency oscillations were observed over regions with a lot of silver conductive paste. The hydrophone was placed to try to minimize this effect as well, while maintaining high amplitude in the frequency region of interest. The entire setup is shown in figure 5.1.

5.2 Test results

A single averaged measurement was done for every damping method for every driving waveform. To better be able to analyse the damping of the signal at the primary resonance frequency, the measurements were band-pass filtered from 200kHz to 600kHz in Matlab. The resulting frequency spectrum can now be analysed to determine the Q-factor. Q-factor is generally calculated according to the formula $Q = \frac{f_c}{B}$ Where f_c is the frequency where the amplitude is maximal, and B the bandwidth. However, due to the flat peaks observed in the frequency spectra, the exact value of f_c was deemed unreliable. Therefore it was decided to use f_{mid} instead of f_c, where f_{mid} is the frequency exactly in the center of the bandwidth. This defines the Q-factor as

$$Q = \frac{f_{mid}}{B} \tag{5.2}$$

The raw and band-pass filtered recordings for the single pulse and counterpulse driving waveform can be seen in figure 5.2 and figure 5.3 respectively and are discussed below.

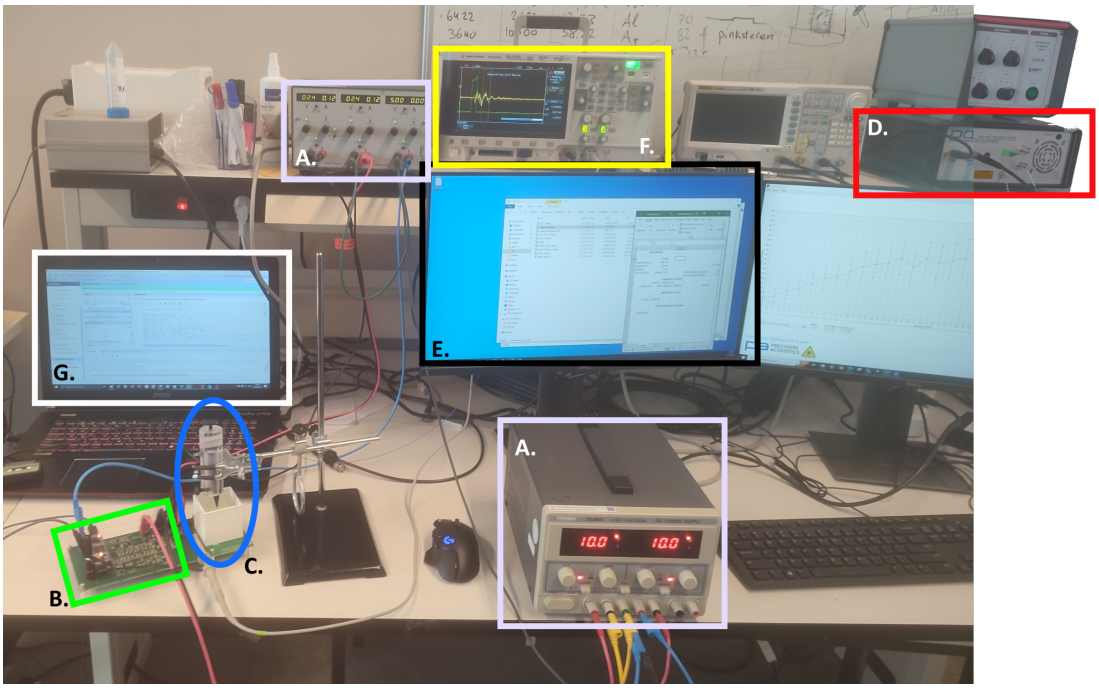

Figure 5.1: Hydrophone measurement setup. **A.**: Power supplies for 5V, ±10V, ±2.4V and ground connection. **B.**: PCB circuit and mounted FPGA. **C.**: Ultrasound transducer in water tank filled with demineralized water. Hydrophone is placed inside water tank to hover over the transducer. **D.**: Precision Acoustics fibre-optic hydrophone system recieves measurement data from the hydrophone via fibre-optic cable. It outputs measurement data via coax to the oscilloscope. **E.**: PC starts the fibre-optic hydrophone system measurement via USB connection. **F.**: The oscilloscope recieves and displays hydrophone data on channel 1. Channel 2 is connected to a probe over the transducer voltage to use as a trigger. **G.**: A USB-stick is used to collect the data from the oscilloscope and transfer it to the user laptop for further processing.

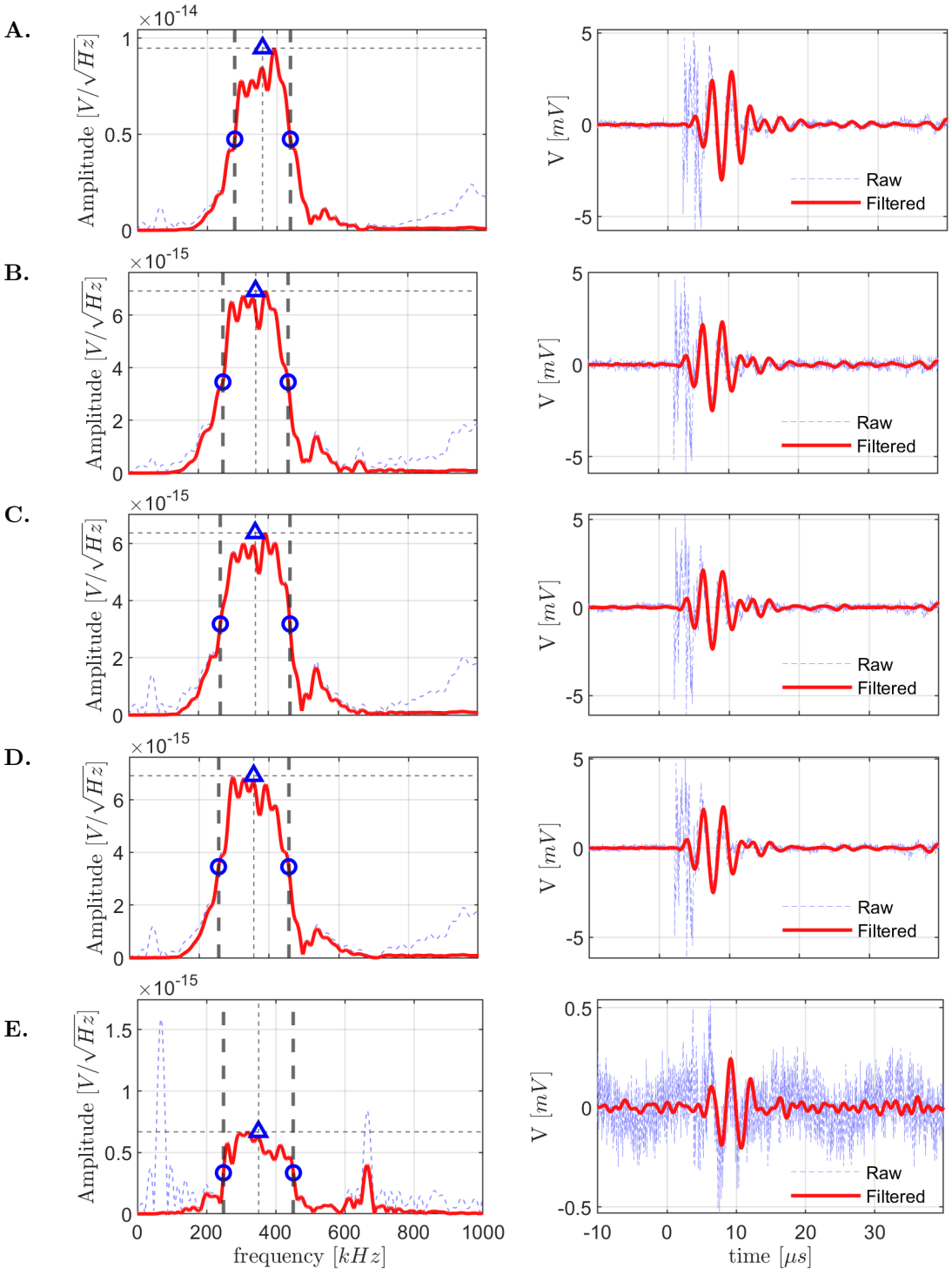

Figure 5.2: Hydrophone recordings for a single pulse driving waveform. Left: amplitude spectrum. Right: time domain recording. The bandwidth is indicated by the two circle markers. Frequency f_{mid} is indicated by the triangle marker. X-axis is the same within every column. **A.**: no damping, **B.**: R-damping, **C.**: inductor simulator, **D.**: RL-damping, **E.**: Proposed Feedback Q-control.

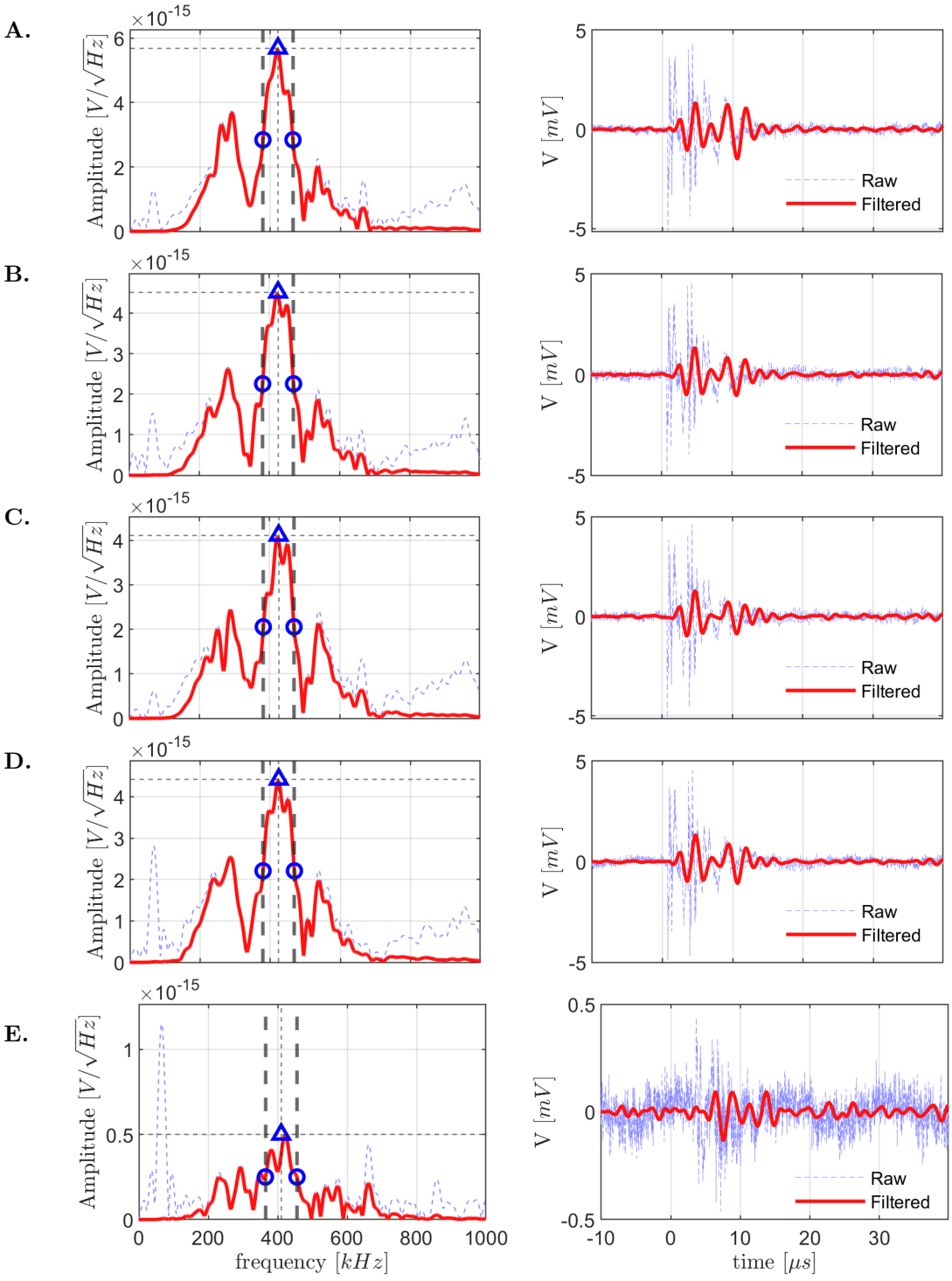

Figure 5.3: Hydrophone recordings for a counterpulse driving waveform. Left: amplitude spectrum. Right: time domain recording. The bandwidth is indicated by the two circle markers. Frequency f_{mid} is indicated by the triangle marker. X-axis is the same within every column. **A.**: no damping, **B.**: R-damping, **C.**: inductor simulator, **D.**: RL-damping, **E.**: Proposed Feedback Q-control.

The lower amplitude for the measurements on the proposed feedback Q-control circuit is caused by the fact that the Feedback driver is driven by a lower voltage, limited by the FPGA output swing, than the Driver subcircuit which has a $\pm 10V$ swing. This is why the observed SNR is lower, not due to increased noise but due to decreased signal amplitude. The Q-factor of a transducer is not dependant on its vibrational amplitude so the comparison between damping modes is still valid. For the counterpulse results in figure 5.3 it appears that the driving waveform causes an overshoot, and the resulting output waves are actually longer than for the single pulse. Other than that, the differences for each damping method are not immediately obvious. To analyze the results, for each damping mode the Q-factor was calculated based on equation 2.13. The used Matlab code can be found on Github [41]. The results are collected in the bar chart of figure 5.4. Both the feedback driver and all shunts

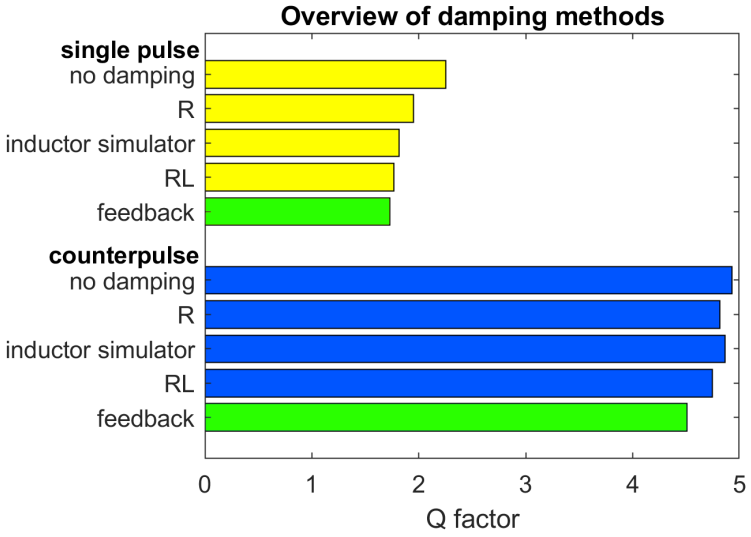

Figure 5.4: Summary of the processed hydrophone measurements. The corresponding Q-factor is shown for each driving waveform (single pulse/counterpulse) and possible additional damping method. 'no damping' is the waveform directly applied to the transducer by the driver subcircuit. R, RL and 'inductor simulator' are the variations of shunts connected to the transducer after transducer excitation by the driver. 'feedback' is the transducer driven by the proposed feedback driver subcircuit which receives either of the driving waveforms as input, and provides the best damping in both cases.

are able to successfuly reduce the transducer's Q-factor. The worst performing method is the counterpulse with no added damping. The highest damping is achieved by the proposed feedback Q-factor control circuit for a single pulse, which yields a Q-factor of 1.73 as compared to 2.25 for single pulse with no damping. This is means an improved axial resolution of approximately $\frac{2.25-1.73}{2.25} = 23\%$. The improvement would most likely be more significant when applying the electronic damping to transducers in a real therapeutic ultrasound array for several reasons. Most importantly, the Q-factor of the mounted transducer was already very low to begin with, much lower than desired for a transducer meant for stimulation purposes. This is because both the water and the PCB already provided a lot of damping. Usually such a transducer would have air-backing, in contrast to being directly mounted on a PCB. Furthermore there would be one or multiple matching layers to improve the transfer from the transducer to the tissue or in this case the water. Another reason is the fact that the damping methods were based on the BVD-model, which is not an entirely complete representation of a piezoelectric transducer. Therefore simulations will also show better results than the real measurements. The counterpulse did not work as expected for this same reason. The used transducer model did not include any mechanism that causes the 'ramp-up' of the oscillation clearly observed in figure 5.2, where the oscillation first grows to a maximum before diminishing again. This behaviour makes the counterpulse actually counterproductive. It only prolongs the oscillation further.

5.3 Discussion

Shunt damping can be improved further by using more accurate shunt values. Even though the calculated shunt values are optimal for the unloaded transducer, mechanical influences were not accounted for. Therefore shunt values were not optimal and there is some room for improvement. RL-damping does slightly outperform R-damping as was expected. The inductor simulator performs slightly worse compared to RL-damping, which makes sense as it can not perfectly replicate the behaviour of the inductor.The feedback driver has much higher damping potential. As displayed by equation 3.24, the feedback factor can be controlled by resistors R_a, R_b and R_c. This factor had to be limited due to the limited range of the opamps. Too high of an amplification factor would cause clipping due to brief voltage peaks, which would saturate the feedback loop. Allowing more headroom for the opamps, and reducing the peak amplitudes at the input of the difference amplifier would both allow for a greater amplification factor. A greater amplification factor leads to increased feedback which leads to improved damping performance. The feedback circuit can be improved further by placing a switch in the feedback path from U3 to U4 in figure 3.10. The simulations in figure 3.11 show that the peak amplitude reduces significantly with increased damping. By only closing the switch after one input cycle, the maximum signal amplitude will be maintained while still maintaining a low Q-factor.
A problem in comparing the feedback driver with the other damping methods is that because of the choice of components, the operating voltage of the feedback driver is four times lower than that of the $\pm 10V$ driver. Even though the Q-factor is not mathematically related to the driving amplitude, it can still be argued that the feedback driver is operating under different conditions and therefore the comparison with other methods is not completely fair. The operating range of the feedback driver was limited by the choice of opamps. The LTC6268 was chosen because of its ultra-low input capacitance. However based on equation 3.21 and 3.22, a higher valued C_b could have been used, allowing for a higher opamp input capacitance than $\mathcal{O}$(100fF). This would have allowed for a wider selection of opamps, possibly with a wider supply range.
In terms of power supply, both voltage converters failed for different reasons. 2.4V plus and minus terminals were swapped in the opamp footprint. The $\pm 2.4V$ converter had to be removed. The 10V converter was removed because it was not designed for such high current draw. The issue was resolved by applying the voltages with the use of external power supplies.
Future research should focus on application of the feedback driver on an air-backed transducer array. Furthermore, as the counterpulse did not prove successful in this thesis, further research can be done on modified waveforms for ultrasound transducer damping. Driving waveforms from Persson et al. [35] should be formalized based on accurate transducer models. Lastly, this thesis has shown implementation on a PCB, but not yet on an Integrated Circuit. Upcoming work should aim to apply electronic damping circuits on an IC.

Chapter 6

Conclusion

A PCB was designed, developed and tested for damping the response of a mounted 4x4x1mm PZT ultrasound transducer. The vibration was measured by means of a hydrophone after submerging the transducer in water. With respect to transducer driving without electronic Q-factor control enabled, a maximum relative damping of 23% was achieved by the proposed Feedback Q-factor control system, improving the theoretical axial resolution by the same amount. This method shows a novel way of damping ultrasonic transducers and has the potential to be extended into applications for entire ultrasonic transducer arrays. Furthermore it was shown that by increasing the gain in the feedback loop, damping can be increased even further if necessary. Lastly, the feedback circuit can be improved with the addition of a switch, preventing reduction of the maximum signal amplitude. A reduction of the Q-factor was also achieved for shunt damping with a resistor, resistor-inductor combination and a resistor-inductor-simulator circuit. Damping by modifying the driving waveform was not successful despite previous studies on this subject. In conclusion this thesis has shown that feasible solutions exist for the electronic Q-factor control of ultrasound transducers, with the potential to be applied on entire transducer arrays. Future work should aim to:

- *apply the feedback driver to an air-backed transducer array*

  This contains two parts. Firstly the efficacy needs to be shown for air-backed transducers, which is what the damping circuit is ultimately designed for. In this situation the damping performance should become much more apparent as compared to this thesis due to the air-backing in contrast to direct mounting on a PCB. Secondly in application on a transducer array it must be demonstrated that the proposed feedack Q-factor control circuit is indeed extendable to many transducers with consistent and good results.

- *expand on the feasibility of modified driving waveforms for transducer damping*

  Where this thesis was unsuccessful in achieving good damping with modified waveforms, previous research does show it can be effective. A challenge in developing this is making it adaptive to different transducers, something which the proposed feedback Q-factor control circuit is more capable of. Each array may require a different shape of driving waveform, so solutions should be based on a more fundamental understanding than current research is. If this can be done it may eventually still prove a better method than the feedback Q-control circuit that was proposed.

- *implement the damping system on an IC*

  For eventual use in medical devices and research, miniturization by implementation in an Integrated Circuit is essential. Here it may become possible to optimize the implementation of the opamps in the proposed feedback Q-factor control circuit to allow for a higher gain and thus even higher damping. Successful miniturization will enable accelerated research in the field of ultrasound neuromodulation and other therapeutic ultrasound techniques and is another step in the direction of wearable therapeutic ultrasound devices in humans.

Appendix A

Altium circuit designs

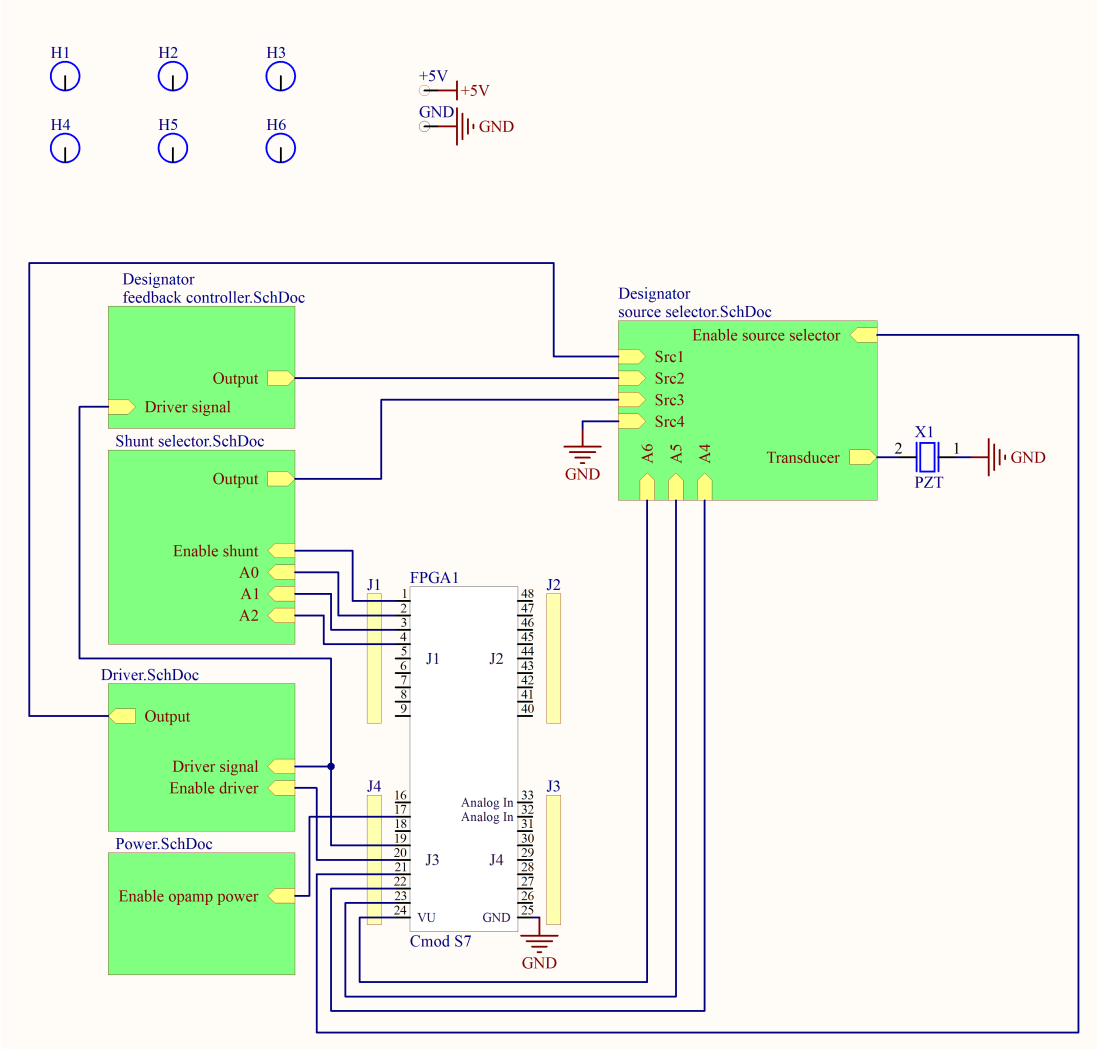

Figure A.1: Top level circuit

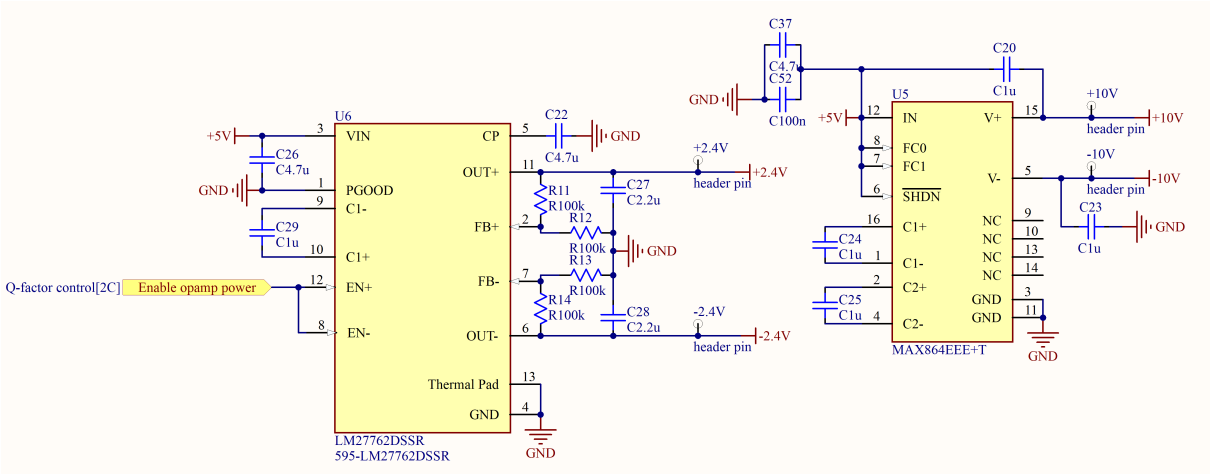

Figure A.2: Power supply unit

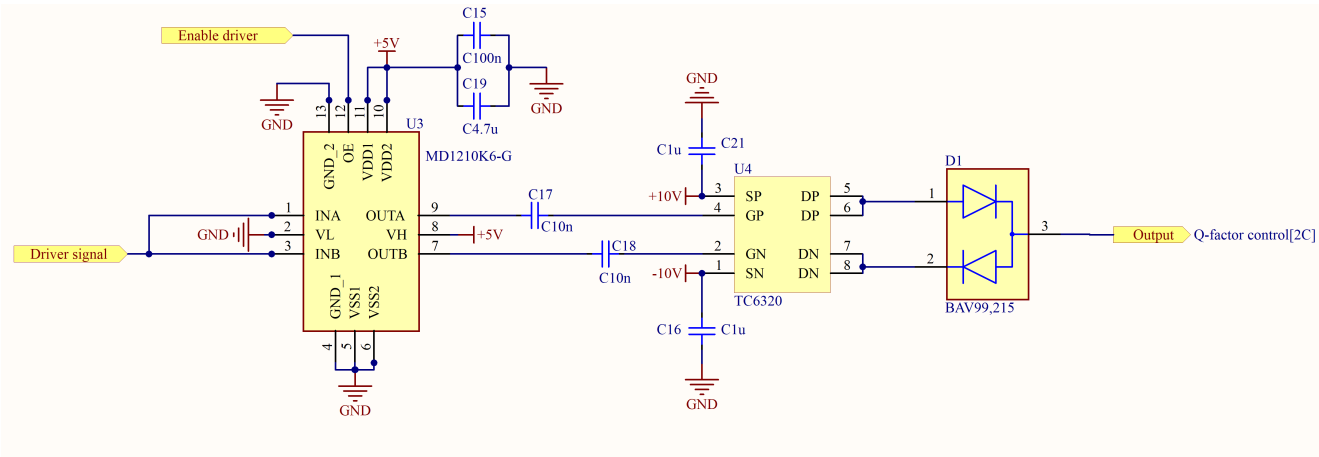

Figure A.3: Transducer driver circuit

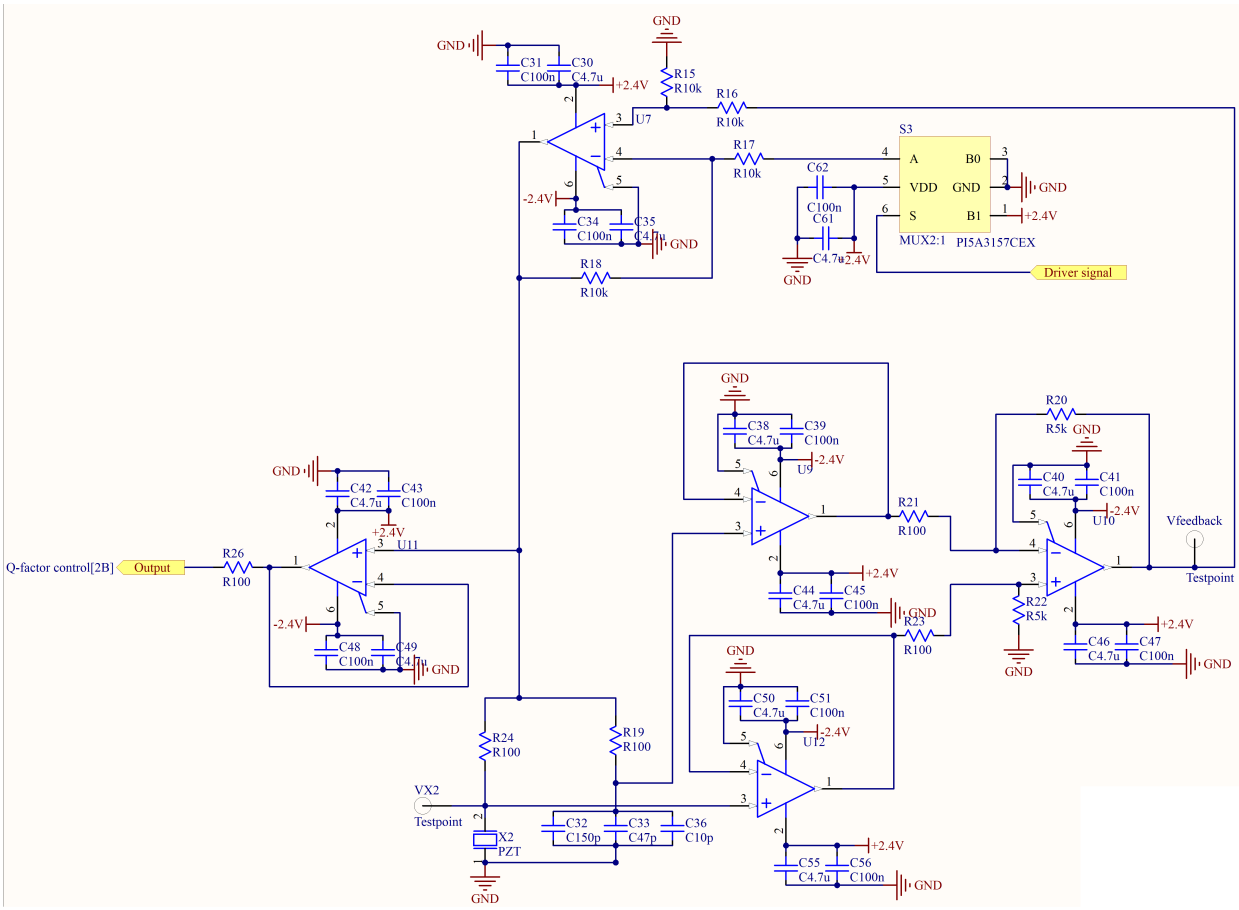

Figure A.4: Feedback driver circuit

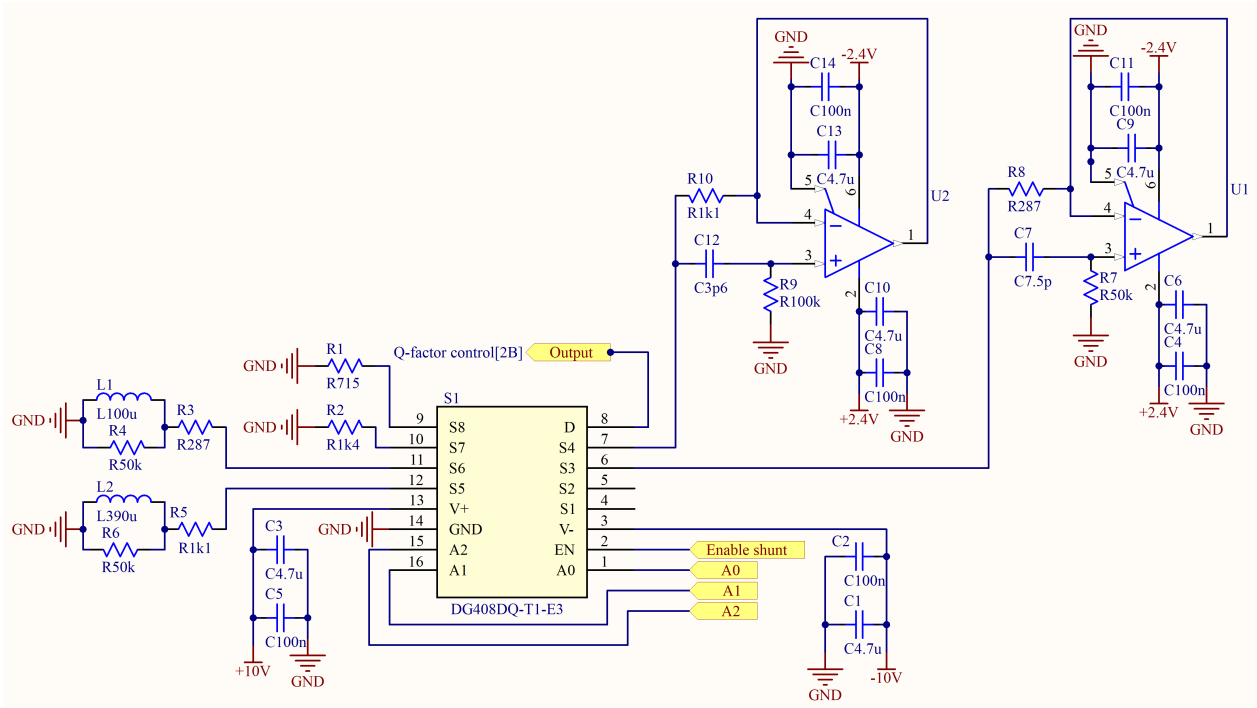

Figure A.5: Shunt selector

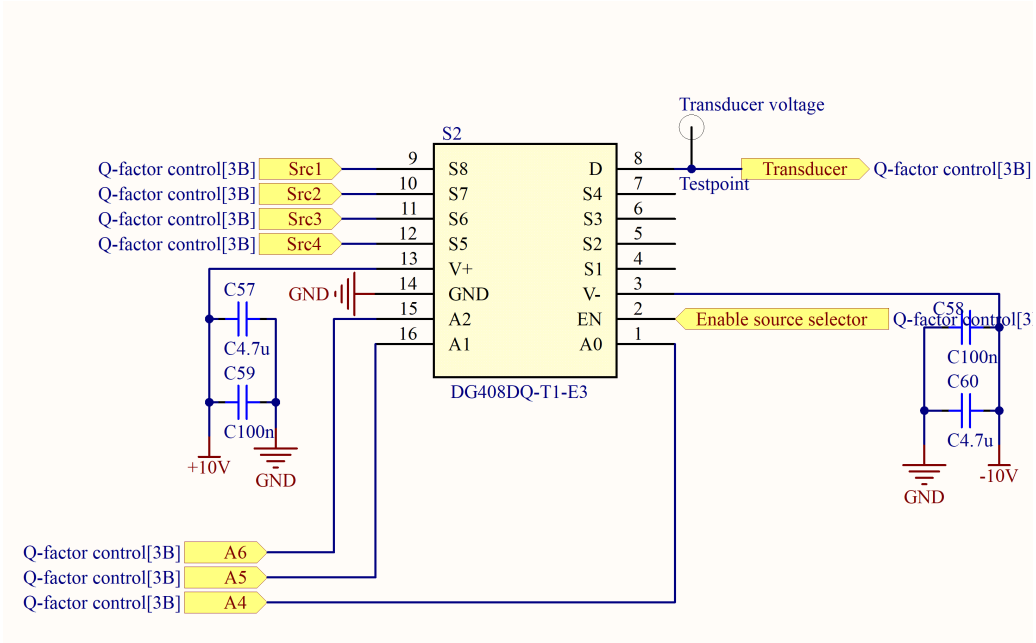

Figure A.6: Source selector

Bibliography

[1] I. Donald, J. Macvicar, and T. Brown, "Investigation of abdominal masses by pulsed ultrasound," *The Lancet*, vol. 271, no. 7032, pp. 1188–1195, 1958, originally published as Volume 1, Issue 7032. [Online]. Available: https://www.sciencedirect.com/science/article/pii/S0140673658919056

[2] A. Copelan, J. Hartman, M. Chehab, and A. M. Venkatesan, "High-intensity focused ultrasound: current status for image-guided therapy," in *Seminars in interventional radiology*, vol. 32, no. 04. Thieme Medical Publishers, 2015, pp. 398–415.

[3] D. L. Miller, N. B. Smith, M. R. Bailey, G. J. Czarnota, K. Hynynen, I. R. S. Makin, and B. C. of the American Institute of Ultrasound in Medicine, "Overview of therapeutic ultrasound applications and safety considerations," *Journal of Ultrasound in Medicine*, vol. 31, no. 4, pp. 623–634, 2012. [Online]. Available: https://onlinelibrary.wiley.com/doi/abs/10.7863/jum.2012.31.4.623

[4] V. Pashaei, P. Dehghanzadeh, G. Enwia, M. Bayat, S. J. A. Majerus, and S. Mandal, "Flexible body-conformal ultrasound patches for image-guided neuromodulation," *IEEE Transactions on Biomedical Circuits and Systems*, vol. 14, no. 2, pp. 305–318, 2020.

[5] G. Li, W. Qiu, J. Hong, Q. Jiang, M. Su, P. Mu, G. Yang, Y. Li, C. Wang, H. Zhang, and H. Zheng, "Imaging-guided dual-target neuromodulation of the mouse brain using array ultrasound," *IEEE Transactions on Ultrasonics, Ferroelectrics, and Frequency Control*, vol. 65, no. 9, pp. 1583–1589, 2018.

[6] J. Kovacs, "Episode 3 - ultrasound." [Online]. Available: https://intro-biomedical-imaging.weebly.com/episode-3---ultrasound.html

[7] M.-A. d'Anjou, "Shape of the ultrasound beam in depth," Mar 2020. [Online]. Available: https://smallanimalultrasonography.com/shape-of-the-ultrasound-beam-in-depth/

[8] D. Maresca and G. Renaud, "Ap 3531 acoustical imaging: Medical ultrasound image reconstruction," April 2022. [Online]. Available: https://brightspace.tudelft.nl/d2l/le/content/398514/viewContent/2646905/View

[9] M. Postema, *Fundamentals of medical ultrasonics*. London, England: CRC Press, Apr. 2014.

[10] J. C. Simon, A. D. Maxwell, and M. R. Bailey, "Some work on the diagnosis and management of kidney stones with ultrasound," *Acoust. Today*, vol. 13, no. 4, pp. 52–59, 2017.

[11] S. A. Alkahtani, P. S. Kunwar, M. Jalilifar, S. Rashidi, and A. Yadollahpour, "Ultrasound-based techniques as alternative treatments for chronic wounds: a comprehensive review of clinical applications," *Cureus*, vol. 9, no. 12, 2017.

[12] V. Velling and S. Shklyaruk, "Modulation of the functional state of the brain with the aid of focused ultrasonic action," *Neuroscience and behavioral physiology*, vol. 18, pp. 369–375, 1988.

[13] J. Li, Y. Ma, T. Zhang, K. K. Shung, and B. Zhu, "Recent advancements in ultrasound transducer: From material strategies to biomedical applications," *BME Front.*, vol. 2022, p. 9764501, May 2022.

[14] N. Ghadarah and D. Ayre, "A review on acoustic emission testing for structural health monitoring of polymer-based composites," *Sensors*, vol. 23, no. 15, 2023. [Online]. Available: https://www.mdpi.com/1424-8220/23/15/6945

[15] W. P. Mason, "Electromechanical transducers and wave filters," 1948. [Online]. Available: https://ia601509.us.archive.org/13/items/in.ernet.dli.2015.13601/2015.13601.Electromechanical-Transducers-And-Wave-Filters_text.pdf

[16] M. M. Ghanbari and R. Muller, "Optimizing volumetric efficiency and backscatter communication in biosensing ultrasonic implants," *IEEE Transactions on Biomedical Circuits and Systems*, vol. 14, no. 6, pp. 1381–1392, 2020.

[17] D. Berlincourt, "Piezoelectric crystals and ceramics," in *Ultrasonic transducer materials*. Springer, 1971, pp. 63–124. [Online]. Available: https://link.springer.com/chapter/10.1007/978-1-4757-0468-6_2

[18] W. M. van Spengen, "The electromechanical damping of piezo actuator resonances: Theory and practice," *Sensors and Actuators A: Physical*, vol. 333, p. 113300, 2022.

[19] M. Redwood, "Transient performance of a piezoelectric transducer," *The journal of the acoustical society of America*, vol. 33, no. 4, pp. 527–536, 1961.

[20] J. van Deventer, T. Lofqvist, and J. Delsing, "Pspice simulation of ultrasonic systems," *ieee transactions on ultrasonics, ferroelectrics, and frequency control*, vol. 47, no. 4, pp. 1014–1024, 2000.

[21] D. K. Cheng *et al.*, *Field and wave electromagnetics*. Pearson Education India, 1989.

[22] W. M. Leach, "Controlled-source analogous circuits and spice models for piezoelectric transducers," *IEEE Transactions on Ultrasonics, Ferroelectrics, and Frequency Control*, vol. 41, no. 1, pp. 60–66, 1994.

[23] Z. Shen, J. Xu, Z. Li, Y. Chen, Y. Cui, and X. Jian, "An improved equivalent circuit simulation of high frequency ultrasound transducer," *Frontiers in Materials*, vol. 8, 2021.

[24] S. A. Morris and C. G. Hutchens, "Implementation of mason's model on circuit analysis programs," *IEEE transactions on ultrasonics, ferroelectrics, and frequency control*, vol. 33, no. 3, pp. 295–298, 1986.

[25] M. Ali and A. R. Mohamed, "A simulation of pulse-echo amplitude scan signal formation in absorbing media," *Ultrasonics*, vol. 30, no. 5, pp. 311–316, 1992.

[26] M. Ali, "Analysis of broadband piezoelectric transducers by discrete time model," *Egypt. J. Sol.*, vol. Vol. (23), No. (2), (2000) 287, p. 287, 01 2000.

[27] C. Hou, C. Fei, Z. Li, S. Zhang, J. Man, D.-D. Chen, R. Wu, L. Di, Y. Yang, and W. Feng, "Optimized backing layers design for high frequency broad bandwidth ultrasonic transducer," *IEEE transactions on biomedical engineering*, vol. PP, 07 2021.

[28] R. E. McKeighen, "Design guidelines for medical ultrasonic arrays," in *Medical Imaging 1998: Ultrasonic Transducer Engineering*, K. K. Shung, Ed., vol. 3341, International Society for Optics and Photonics. SPIE, 1998, pp. 2 – 18. [Online]. Available: https://doi.org/10.1117/12.307992

[29] S. Behrens, A. Fleming, and S. Moheimani, "A broadband controller for shunt piezoelectric damping of structural vibration," *Smart materials and structures*, vol. 12, no. 1, p. 18, 2003.

[30] S. yau Wu, "Piezoelectric shunts with a parallel r-l circuit for structural damping and vibration control," in *Smart Structures*, 1996.

[31] S. Behrens and S. R. Moheimani, "Optimal resistive elements for multiple mode shunt damping of a piezoelectric laminate beam," in *Proceedings of the 39th IEEE Conference on Decision and Control (Cat. No. 00CH37187)*, vol. 4. IEEE, 2000, pp. 4018–4023.

[32] K. Marakakis, G. K. Tairidis, P. Koutsianitis, and G. E. Stavroulakis, "Shunt piezoelectric systems for noise and vibration control: a review," *Frontiers in Built Environment*, vol. 5, p. 64, 2019.

[33] J. Yen and Z. Nussbaum, "Active damping of air-backed ultrasonic transducers using arbitrary waveform generators," in *2020 IEEE International Ultrasonics Symposium (IUS)*, 2020, pp. 1–4. [Online]. Available: https://doi.org/10.1109/IUS46767.2020.9251816

[34] G. Kossoff, "The effects of backing and matching on the performance of piezoelectric ceramic transducers," *IEEE Transactions on Sonics and Ultrasonics*, vol. 13, no. 1, pp. 20–30, 1966.

[35] H. W. Persson, "Electric excitation of ultrasound transducers for short pulse generation," *Ultrasound in Medicine Biology*, vol. 7, no. 3, pp. 285–291, 1981. [Online]. Available: https://www.sciencedirect.com/science/article/pii/0301562981900399

[36] C.-M. Chen and B. Choubey, "Ultrasound transducer quality factor control using coupled external electrical resonator," in *2018 IEEE SENSORS*, 2018, pp. 1–4.

[37] X. WU, T. REN, and L. LIU, "Active damping of a piezoelectric mems acoustic sensor," *Integrated Ferroelectrics*, vol. 80, no. 1, pp. 317–329, 2006. [Online]. Available: https://doi.org/10.1080/10584580600660108

[38] T. Connectivity, "SDT Shielded Piezo Sensors," https://www.te.com/commerce/DocumentDelivery/DDEController?Action=showdoc&DocId=Data+Sheet%7FSDT_Shielded_Piezo_Sensors%7FA1%7Fpdf%7FEnglish%7FENG_DS_SDT_Shielded_Piezo_Sensors_A1.pdf%7F11031263-00, 2023, [Online; accessed 14-November-2023].

[39] W. Wong, C. Christoffersen, S. Pichardo, and L. Curiel, "An integrated ultrasound transducer driver for hifu applications," in *2013 26th IEEE Canadian Conference on Electrical and Computer Engineering (CCECE)*, 2013, pp. 1–5.

[40] R. Queirós, P. S. Girão, and A. C. Serra, "Single-mode piezoelectric ultrasonic transducer equivalent circuit parameter calculations and optimization using experimental data," in *IMEKO TC4 International Symposium on New Technologies in Measurement and Instrumentation*, vol. 2, no. 1, 2005, pp. 468–471.

[41] T. F. Wemelsfelder, "Master thesis repository," 2024, accessed: January 21, 2024. [Online]. Available: https://github.com/tomwemelsfelder/Master-Thesis

[42] V. Upadhye and S. Agashe, "Effect of temperature and pressure variations on the resonant frequency of piezoelectric material," *Measurement and Control*, vol. 49, no. 9, pp. 286–292, 2016. [Online]. Available: https://doi.org/10.1177/0020294016663974

[43] "High-speed dual mosfet driver - microchip technology," 2020. [Online]. Available: https://ww1.microchip.com/downloads/en/DeviceDoc/MD1210-High-Speed-Dual-MOSFET-Driver-Data-Sheet-200056pdf